Construction of Temperature Climate Data Records in the Upper Troposphere and Lower Stratosphere Using Multiple RO Missions from 2006 to 2023 at NESDIS/STAR

Jun Zhou[1], Shu-Peng Ho[2], Xinjia Zhou[1], Xi Shao[1], Guojun Gu[1], Yong Chen[2], and Xin Jing[1]

[1] Cooperative Institute for Satellite Earth System Studies (CISESS), Earth System Science Interdisciplinary Center, University of Maryland, College Park, MD 20740, USA.

[2] NOAA/NESDIS/Center for Satellite Applications and Research, 5830 University Research Court, College Park, MD 20740-3818.

Corresponding author: Jun Zhou (jzhou128@umd.edu)

Key Points:

- A new temperature monthly mean climatology (MMC) was developed based on multiple GNSS RO missions processed by NOAA STAR.
- Sampling errors in MMC were corrected and the sampling error correction method was validated through three different reanalysis models.
- The STAR MMC exhibited good agreement with the ROM SAF MMC, and the MMC derived from ERA-5, MERRA-2, and JRA-55 reanalyses.

Abstract

We develop a new gridded monthly mean climatology (MMC) in the upper troposphere and lower stratosphere (UTLS) from 2006 to 2023 using the dry temperature profiles from multiple Global Navigation Satellite System (GNSS) Radio Occultation (RO) missions processed by the GNSS RO Science and Data Center (SDC) at the NOAA Center for Satellite Applications and Research (STAR). The multiple RO missions include Formosa Satellite Mission 3/Constellation Observing System for Meteorology, Ionosphere, and Climate (COSMIC-1), Formosa Satellite Mission 7/ COSMIC-2, SPIRE, and Meteorological Operational satellite (MetOp)-A, -B, -C. The sampling error in MMC is corrected by using ERA-5 reanalysis. The robustness of the sampling error correction method is validated through three different reanalysis models. The result shows that the mission difference in MMC is significantly reduced after sampling error correction, and the uncertainty caused by using different models in the correction method can be neglected. This STAR MMC is then compared with the ROM SAF MMC and the MMC derived from ERA-5, MERRA-2, and JRA-55 reanalyses, exhibiting good agreement. Various climate signals, such as Quasi-Biennial Oscillation (QBO) and El Niño–Southern Oscillation (ENSO), can be identified from STAR MMC. The global temperature trends present a transition from a prominent warming of 0.309 ± 0.085 K/Decade in the upper troposphere to a robust cooling of -0.281 ± 0.044 K/Decade in the mid-stratosphere, consistent with the well-known response of the UTLS region to long-term global warming. These results demonstrate that STAR MMC can capture climate signals and monitor long-term climate change.

Plain Language Summary

The detailed structure of upper-air temperature variability is vital for a better understanding climate change and its causes. Substantial efforts have been made to construct consistent and reliable climate data records from various observational systems and models. However, discrepancies remained in the upper troposphere and lower stratosphere (UTLS) region. Global Navigation Satellite System (GNSS) Radio Occultation (RO) provides new insights into the fine temperature structure in the UTLS region with high vertical resolution, accuracy, and long-term stability. In this study, we develop a new gridded monthly mean climatology (MMC) in the UTLS using the temperature profiles from multiple GNSS RO missions processed by the GNSS RO Science and Data Center (SDC) at the NOAA Center for Satellite Applications and Research

(STAR). STAR MMC is generated by binning and averaging the RO profiles on 2D latitude-height grids with a resolution of 5º in latitude by 0.2 km in height. This STAR MMC is validated by comparing it with the MMC generated by another independent center and the MMC derived from various reanalysis models. The comparison exhibits good agreement between STAR MMC and other datasets. The results demonstrate that STAR MMC can capture climate signals and monitor long-term climate change.

1 Introduction

The atmospheric temperature in the upper troposphere and lower stratosphere (UTLS) provides a clear fingerprint of global warming signals, reflecting both natural and anthropogenic forcings (Rohli and Vega 2017). An accurate UTLS temperature trend estimate with high vertical resolution and global coverage is vital to understanding climate variation and verifying climate model simulations. However, documenting the strong vertical gradient in UTLS temperature has been challenging in both observations and models (Eyring et al., 2016; Santer et al., 2017; Ladstädter et al., 2023).

In the past 40 years, spaceborne microwave (MW) radiometers and radiosonde observations (RAOBs) have been the primary data sources for upper-air temperature trend detection. However, the layer-averaged measurements from MW sounders can hardly resolve the crucial vertical detail structure around the UTLS region, while the RAOBs data is mostly limited to regions over land. In addition, evaluating long-term temperature changes from these platforms is challenging owing to the trend uncertainties caused by the instrument changes over time, changes in the observational network, and inconsistent calibration and correction approaches of the inter-satellite offsets among missions. Various reanalysis datasets were used to investigate temperature variabilities. However, their representation of temperature in the UTLS might be problematic due to the lack of high-quality and high-vertical-resolution temperature observations and the low vertical resolution of the model (Zhao and Li, 2006; Trenberth and Smith, 2006,2009; Shangguan et al., 2019). Substantial efforts have been put into the homogenization and inter-calibration procedures for the construction of climate data records (Titchner et al., 2009; Haimberger et al. 2008, 2012; Spencer et al. 2017; Mears and Wentz, 2017; Zou et al. 2023), but discrepancies between temperature trends from various observational systems and models remained in the UTLS region (Fu et al. 2011; Mitchell et al. 2013, Ladstädter, 2023).

The consistent and detailed structure of temperature trends in UTLS is essential for climate studies. For example, there has been a considerable scientific and political dispute about the extent of temperature change in the atmosphere (Ladstädter, 2023) and a debate over ozone recovery in the lower stratosphere due to the Montreal Protocol (Ball et al., 2018). The capability of resolving the stratosphere-troposphere coupling is required to better understand the strong impact of the stratosphere on the troposphere and even surface weather and climate (Kidston et al., 2015). The temperature of the tropical tropopause layer (TTL) needs to be resolved since it plays an essential role in controlling the amount of water vapor entering the stratosphere, which can further determine climate sensitivity and feedback on the TTL (Solomon et al., 2010; Birner and Charlesworth, 2017; Charlesworth et al., 2019).

As a complement to MW sounders and RAOBs, Global Navigation Satellite System (GNSS) Radio Occultation (RO) data are increasingly making essential contributions to weather forecasting (Healy et al., 2005; Cardinali and Healy, 2014), atmospheric studies (Poli et al., 2010), and climate monitoring (Steiner et al.,2011; Anthes, 2011, Ho et al. 2009; Ho et al. 2019, 2022). RO is an active limb-sounding technique based on the refraction of GNSS radio signals by the atmospheric refractivity field during their propagation to a receiver on a low-earth orbit satellite (ROM SAF ROPP, 2021; Dach et al., 2015). Compared to traditional observing techniques, it offers several advantages that make it well suited for climate studies, especially for UTLS temperature monitoring: i) it provides geophysical profiles with high vertical resolution and global coverage throughout the troposphere and stratosphere (Kursinski et al. 1997; Zeng et al. 2019), ii) it is insensitive to clouds and the underlying surface, and iii) it has intrinsic long-term stability that allows different missions to be combined into a seamless observation record without the need for inter-calibration or temporal overlap (Leroy et al., 2006, Steiner et al. 2020a).

The assessments of the consistency and long-term stability of RO observations for use as climate data records (CDRs) in previous studies (Ho et al. 2009; Ho et al. 2019, 2022) concluded that RO records can be used for reliable climate trend assessments globally in the UTLS region, meeting the stringent Global Climate Observing System (GCOS) program stability requirements (Scherllin-Pirscher, 2011, Steiner et al. 2013, 2020a). Recently, GNSS RO has been widely used to estimate upper-air temperature trends, which have been verified through comparison with various observation and model systems (Khaykin et al. 2017; Leroy et al. 2018; Steiner et al. 2020b; Vergados et al. 2021; Gleisner 2020, 2022; Ladstädter et al. 2023).

As Steiner et al. (2020a) pointed out, the uncertainty in RO observational records stems from different choices in processing and methodological approaches for constructing a data set from the same raw data. Therefore, multiple independent efforts should be undertaken to create climate records to quantify the true spread of possible physical solutions. The NOAA Center for Satellite Applications and Research (STAR) has recently developed capabilities as a GNSS RO science and data center (STAR RO DSC). Like other NOAA's infrared and microwave satellite missions, we aim to establish enterprise RO processing algorithms for all RO missions.

At STAR RO DSC, the Radio Occultation Processing Package (ROPP) has been reconfigured to accommodate various GNSS missions, including Global Positioning System—GPS, GALILEO, and GLObal NAvigation Satellite System—GLONASS, making it especially well-suited for the new generation of RO missions like Constellation Observing System for Meteorology, Ionosphere, and Climate-2 (COSMIC-2) and commercial CuteSats from SPIRE Inc. This STAR-reconfigured ROPP is used to consistently produce the RO bending angle, refractivity, and dry temperature profiles from multiple RO missions, including Constellation Observing System for Meteorology, Ionosphere, and Climate (COSMIC-1), COSMIC-2, SPIRE, Meteorological Operational Satellite-A (Metop-A), -B, and -C. These RO profiles compose the STAR-ROPP dataset from April 2006 to July 2023.

This study aims to combine the dry temperature profiles from the STAR-ROPP post-processed dataset to construct the temperature climate data records (CDRs) at 8-30 km from 2006 to 2023. UTLS is usually defined as the region ± 5 km of the tropopause. We focus on a broader region from the upper troposphere to the mid-stratosphere because this is a core region where GNSS RO temperature data is of good quality (Ho et al. 2009; Schmidt et al. 2010; Steiner et al. 2020a). Because RO measurements from the above missions are of different temporal and spatial coverages, we must first remove the sampling errors to generate consistent monthly mean climatology (MMC). Here, we use three reanalysis datasets (i.e., fifth-generation European Centre for Medium-Range Weather Forecasts (ECMWF) atmospheric reanalysis (ERA-5), Modern-Era Retrospective analysis for Research and Applications, Version 2 (MERRA-2), and

Japanese 55-year Reanalysis (JRA-55) to estimate the related sampling errors and the uncertainty of the sampling error correction method. Then, the STAR UTLS temperature MMCs are validated by comparing them with the MMCs produced by EUMETSAT RO Meteorology Satellite Application Facility (ROM SAF) within their overlapping period (2006-2016). In addition, to validate their climate monitoring capability, the UTLS temperature trends at different latitude zones and altitude regions are calculated from the STAR MMCs and compared with those obtained from the ERA-5, MERRA-2, and JRA-55 reanalysis datasets.

Section 2 provides an overview of the STAR-ROPP post-processed data used to construct the STAR MMC and the ancillary datasets used for the sampling error correction and MMC evaluation. Section 3 describes the algorithms used to assess the consistency among multiple RO missions, to generate STAR MMC, and to correct the sampling error in MMC. Section 4 shows the results, including validating RO mission consistency, quantifying the uncertainty in the sampling error correction, comparing with ROM SAF MMC, and analyzing the consistency of climatology obtained from STAR MMC and multiple reanalysis datasets.

2 Data

2.1 STAR-ROPP Post-processed GNSS RO Dataset

We have reconfigured the Radio Occultation Processing Package (ROPP) version 10 (ROPP user guide; see ROM SAF ROPP, 2021) to add more capabilities. The reconfigured ROPP, named STAR-ROPP, can restore the high time resolution orbit positions and signal transmission from the low time resolution data provided by the University Corporation for Atmospheric Research (UCAR) and process observations from more GNSS systems such as GLONASS, GALILEO, and BeiDou, in addition to GPS. The latter ability makes it especially well-suited for the new generation of RO sensors like COSMIC-2 and SPIRE. A post-process quality control procedure is implemented to ensure a high-quality dataset. Using STAR-ROPP, we can convert RO excess phase (level1b) data to the bending angle, refractivity, and dry temperature profiles for multiple RO missions. These dry variables approximate the corresponding physical variables throughout the UTLS region where water vapor is negligible (Gleisner et al. 2020). The details of the retrieval algorithm and the configuration parameters used in STAR-ROPP can be found in STAR-ROPP version 1.0 ATBD.

This study uses the dry temperature profiles from the STAR-ROPP processed dataset to construct the MMC in UTLS from 2006 to 2023. This dataset includes profiles from six RO missions: COSMIC-1, COSMIC-2, Metop-A/-B/-C, and SPIRE (only including the RO profiles in NOAA commercial data program (CDP) RO Data Buy). The data coverage of each mission is listed in Table 1.

Table 1

RO Missions and Corresponding Data Coverage

RO mission	Data coverage
SPIRE	Sep 2021 to Jul 2023
COSMIC2	Oct 2019 to Jul 2023
COSMIC1	Apr 2006 to Apr 2020
Metop-A	Oct 2007 to Nov 2021
Metop-B	Feb 2013 to Mar 2023
Metop-C	Jul 2019 to Feb 2023

The six RO missions include over 20 million occultations collected from April 2006 to July 2023. Figure 1 shows the statistics on the valid RO profiles used to generate STAR ROPP MMC. Figure 1 (a) presents the monthly mean daily number of valid profiles for each mission and combined missions. It shows that the daily observation number peaked at well above 5,000 after 2019 when COSMIC-2 data became available. Including SPIRE led to a second peak in the daily data number since 2021. Figure 1 (b) illustrates the latitude distribution of RO profiles for different missions in a specific month. The different spatial coverage among the missions is due to their distinct orbits. With relatively high inclination angles, COSMIC-1 and Metop-A have a global distribution. COSMIC-2 data covers mainly from 45ºS to 45ºN because of its low inclination angle. SPIRE constellation has 112 LEO-based CubeSats in a diverse set of orbits, enabling global spatial distribution. Figure 1 (c) depicts the local time distribution of RO measurements. The Sun-synchronous satellite Metop-A/-B/-C has a fixed equator crossing time of descending node (ECT) at 0930 local time, except that Metop-A gradually drifted to orbit with an ECT of 0750 since 2017. Even though the limb sounding somewhat spreads the local time when the measurements are performed, most measurements are from around 0800-1100 and 2000-2300 local times, and the entire diurnal cycle can never be resolved at low and mid-latitudes. COSMIC-1/2 has six satellites with an orbit drifting rate of about -2º per day, which allows them to sample the complete diurnal cycles of atmospheric temperature within one month. For the SPIRE mission, which consists of Sun-synchronous and non-Sun-synchronous satellites, the full-temperature diurnal cycle can be covered but with higher sampling weights around certain local times. Readers can obtain the STAR-ROPP post-processed GNSS RO dataset at https://gpsmet.umd.edu/star_gnssro/description.html.

2.2 Ancillary Data

2.2.1 ROM SAF Monthly Mean Climatology

This study compares the newly developed STAR UTLS temperature MMC with the MMC from ROM SAF CDR v1.0 during their overlapping time from 2006 to 2016. The ROM SAF CDR v1.0 includes data from four RO missions: CHAMP, GRACE, COSMIC-1, and Metop. The low-level input data for the first three missions was from UCAR, while the input data for Metop was from EUMETSAT. There were version updates of COSMIC-1 and GRACE input data involving low-level processing software changes at UCAR. The input data were processed to geophysical variables using the ROM SAF GNSS Processing and Archiving Center (GPAC) v2.3.0, with the Radio Occultation Processing Package (ROPP) v8.1 as an integral part. The geophysical variables include bending angle, refractivity, dry temperature, dry pressure, dry geopotential height, temperature, specific humidity, and tropopause height. These profiles undergo an area-weighted averaging to form monthly means on 2D latitude-height grids with a resolution of 5 degrees in latitude by 200 meters in mean sea level (MSL) height. Sampling error is reduced from MMC by sub-sampling the ERA5 reanalysis model (Gleisner et al., 2020; ROM SAF level 3 ATBD, 2021). The ROM SAF MMC was downloaded from https://preop.romsaf.org/product_archive.php.

2.2.2 ERA-5

ERA5 reanalysis data is used as a reference in the sampling error correction and in the evaluation of STAR-ROPP MMC, covering the entire observation time from 2006 to 2023. ERA-5 is the latest climate reanalysis produced by ECMWF, following predecessors such as the First Global Atmospheric Research Program Global Experiment, ERA-15, ERA-40, and ERA-I. ERA-5 uses the 4-Dimensional Variational (4D-var) data assimilation technique in the Integrated Forecasting System (IFS) Cy41r2 to reanalyze the archived observations, ensuring the best possible temporal consistency of its products (Hersbach et al. 2020). The atmospheric data has been available with multiple spatial and temporal resolutions since 1940 and continues to be extended forward. The global field of atmospheric temperature with 6-hour intervals (0000, 0600, 1200, 1800 UTC) on a regular 0.25º×0.25º grid and 37 pressure levels is used in this study. Spanning vertically from 1000 hpa to 1 hpa, the ERA-5 temperature field can fully cover the UTLS region. The daily ERA-5 reanalysis data was downloaded from https://cds.climate.copernicus.eu/cdsapp#!/dataset/reanalysis-era5-pressure-levels?tab=overview

2.2.3 MERRA-2

The second Modern-Era Retrospective Analysis for Research and Applications (MERRA-2) is a NASA atmospheric reanalysis that began in 1980. It replaces the original MERRA reanalysis using an upgraded version of the Goddard Earth Observing System Model, Version 5 (GEOS-5) data assimilation system and upgraded atmospheric general circulation model assimilation techniques. These techniques enable the use of observations from newer microwave sounders and hyperspectral infrared radiance instruments (Gelaro et al. 2017). The MERRA-2 products with 3-hour intervals on a regular 0.625º×0.625º grid and 42 pressure levels from 1000 to 0.1 hpa are used in the sampling error correction and STAR MMC evaluation. The MERRA-2 data is accessible online at https://daac.gsfc.nasa.gov.

2.2.4 JRA-55

The Japan Meteorological Agency (JMA) conducted JRA-55, the second Japanese global atmospheric reanalysis project. It covers 55 years, extending back to 1958. Compared to its predecessor, JRA-25, JRA-55 is based on a new data assimilation and prediction system that improves many deficiencies found in the first Japanese reanalysis. These improvements have come about by implementing higher spatial resolution (TL319L60), a new radiation scheme, four-dimensional variational data assimilation (4D-Var) with Variational Bias Correction (VarBC) for satellite radiances, and the introduction of greenhouse gases with time-varying concentrations. The entire JRA-55 production was completed in 2013 and will be continued in real-time (Kobayashi et al. 2015). In this study, JRA-55 is used in sampling error correction and STAR MMC evaluation. The global atmospheric variables with 6-hour intervals (0000, 0600, 1200, 1800 UTC) on a regular 1.25º×1.25º latitude-longitude grid and 37 pressure levels covering 1000 ~ 1 hpa was downloaded from https://jra.kishou.go.jp/JRA-3Q/index_en.html.

3 Algorithm Description

This section briefly describes the process from RO retrieved geophysical profiles to the grided monthly mean data, atmospheric temperature anomaly time series, and temperature trends. The methods of assessing RO mission differences and correcting sampling errors in MMC are also presented.

3.1 Validating Consistency among Missions

Data consistency is an important prerequisite to building RO climatology based on a combined data record from different missions. It enables RO climatology to detect and monitor weak climate trends. To validate the consistency among STAR-ROPP processed RO missions, we combine the Metop-A, -B, and -C into a long-term dataset, Metop, and use it as a reference to validate the consistency of the COSMIC-1, COSMIC-2, and SPIRE datasets. The collocation criteria are set by a time difference of no more than 30 minutes and a horizontal spatial separation of less than 150 km at around 5 km altitude of the tangent point. If more than one profile satisfies these collocation criteria, the one closest to the related profile is chosen, and others are discarded.

Figure 2 (a) shows an example of the global distribution of the collocated pairs of COSMIC-2 and Metop in May 2021. Figure 2 (b) presents the monthly number of the matched profiles for the mission pairs. Of nearly 20 million profiles examined, 30312 coincident pairs were found for COSMIC-1 and Metop, 33532 pairs for COSMIC-2 and Metop, and 33495 pairs for SPIRE and Metop.

The profiles are then interpolated into 8-30 km with 0.2 km intervals, and the difference of the paired profiles at each altitude level is calculated. To obtain robust statistics less sensitive to outliers caused by sharp temporal and spatial temperature variation, we use the median and the 68% confidence interval σ as measures of the mean and standard deviation of the difference (Hajj et al. 2004). The σ is defined as the range centered at the median and contains 68% of the counts, equivalent to the standard deviation in Gaussian distribution. The time series of the monthly median and σ of the mission difference will be calculated at different vertical layers and latitude zones.

3.2 Generating Monthly Zonal Mean Climatology

Monthly zonal mean climatology (MMC) is obtained by binning and averaging the retrieved RO profiles. For this study, MMC is constructed on 2D latitude-height grids with a resolution of 5º in latitude by 0.2 km in height. All the valid RO profiles from the STAR ROPP processed dataset are interpolated onto an equidistant 0.2 km altitude grid. The valid observations that fall within a latitude bin, altitude interval, and calendar month undergo an area-weighted averaging to form the MMC for that specific altitude, latitude, and month. The weighting is done by dividing each latitude bin into two sub-bins, computing an average for each of these, and then computing the mean of the two averages weighted by the areas of the sub-bins.

$$MMC_{obs} = \frac{1}{A}\sum_{s=1}^{2} A_s \cdot \left[\frac{1}{M_s}\sum_{j=1}^{M_s} T_{s,j}\right] \quad (1)$$

where MMC_{obs} denotes the MMC based on RO observations, A_s is the area of the sth sub-bin, M_s is the number of RO temperature observations within the sth sub-bin, and $T_{s,j}$ is the jth observation in the sth sub-bin. This sub-gridding method has been proven to better approximate area-weighted mean for irregularly distributed RO observations (Gleisner, 2011). In this study, only those latitude, height, and month bins containing more than five RO profiles are valid for the MMC calculation. The MMC for individual and combined missions is generated from April 2006 to July 2023. The analysis will focus on the dry temperature MMC covering the UTLS from 8 ~ 30 km.

3.3 Sampling Error Correction

As shown in Figure 1, RO measurements are irregularly distributed in both spatial and temporal domains, resulting in sampling errors in RO climatology. The sampling error is regarded as an important error source in MMC_{obs} that needs to be handled to produce reliable MMC datasets. The sampling error can be estimated and reduced by employing a reanalysis model through the following procedure (Ho et al. 2009; Gleisner et al. 2020):

(1) Interpolating the reanalysis model profiles to the times and locations of each RO profile and generating the sampled monthly mean (MMC_{Int}) following the method described in Section 3.2. MMC_{Int} represents the MMC with sampling error.

(2) Calculating the model monthly mean (MMC_{grid}) by binning and averaging the four-dimensional reanalysis model field with the weight of cosine latitude:

$$MMC_{grid} = \frac{1}{n_t n_\varphi n_\lambda} \cdot \frac{1}{\sum_{k=1}^{n_\varphi} \cos\varphi_k} \cdot \sum_{t=1}^{n_t} \sum_{k=1}^{n_\varphi} \sum_{l=1}^{n_\lambda} T_{tkl} \cos\varphi_k \quad (2)$$

where T_{tkl} and φ_k are the temperature and latitude at a model grid, and the summation loops over all n_t, n_φ, and n_λ time-latitude-longitude model grid points located within the MMC grid box. MMC_{grid} represents the MMC without sampling error.

(3) The MMC sampling error (MSE) is estimated as the difference between MMC_{Int} and MMC_{grid}:

$$MSE = MMC_{Int} - MMC_{grid} \quad (3)$$

(4) The sampling error in MMC_{obs} is corrected by subtracting MSE from MMC_{obs}:

$$MMC_{crr} = MMC_{obs} - MSE \quad (4)$$

In the STAR MMC, sampling errors are estimated from the ERA-5 reanalysis model described in Section 2.2.2. Two additional reanalysis models, JRA-55 and MERRA-2, are also employed to quantify the uncertainty in the sampling error estimation.

Figure 3 shows an example of sampling error correction made for the dry temperature monthly mean from COSMIC-1 in January 2009. As illustrated in Figure 3(c), the positive value of sampling error at high northern latitudes above 12 km is prominent. This is attributable to the combined effect of the wintertime polar vortex and the sparse distribution of COSMIC-1 measurements at high-latitude regions (Figure 1 (b)). It demonstrates that the strong spatiotemporal temperature variability caused by the polar vortex cannot be fully sampled by RO observations, resulting in large sampling errors around the North Pole. Comparison of Figure 3 (a)-(b) shows that after sampling error correction, the abrupt temperature change at high latitude in MMC_{obs} is largely removed, leaving a smoother temperature field in MMC_{crr} around the polar area.

3.4 Temperature anomaly time series and trends

The anomalies are defined as the deviation from a climatological seasonal cycle. The mean seasonal cycle is calculated by averaging data for the same month at each MMC_{crr} grid cell over multiple years. The anomalies are obtained by subtracting the seasonal cycle from MMC_{crr}. The anomalies are a function of latitude, altitude, and time. Averaging over latitude bins with the weight of cosine latitude gives a two-dimensional time-altitude anomaly data set, while averaging over latitude and altitude bins gives a one-dimensional anomaly time series. Trends are computed by applying a linear least square fit to the anomaly time series. The uncertainty estimates of the trends are expressed as a 95% confidence level. Trends are deemed to be significantly different from zero if the confidence interval does not contain the null hypothesis value (Steiner et al., 2020b). For a comparison of anomaly time series and trends from different datasets, the same period should be selected for the seasonal cycle calculation. In this study, only the months when all the latitude bins (90ºS-90ºN) and altitude bins (8-30 km) are valid are included in the temperature anomaly time series and trend calculation.

4 Results

4.1 Assessment of the Consistency among Missions

In this section, we validate the consistency among the STAR-ROPP processed dry temperature profiles from multiple missions by applying the method described in Section 3.1. Figure 4-6 present the time evolutions of the median and 68% confidence interval σ of mission difference at three vertical layers including the upper troposphere (8-12 km), the lower stratosphere including tropopause (12-20 km), and the mid-stratosphere (20-30 km), at six latitude zones including global (90ºS to 90ºN), southern hemisphere polar (90ºS to 60ºS, SHP), southern hemisphere subtropics and midlatitudes (60ºS to 20ºS, SHSM), tropics (20ºS to 20ºN, TRO), northern hemisphere subtropics and midlatitudes (20ºN to 60ºN, NHSM), and northern hemisphere polar (60ºN to 90ºN, NHP). The average of the median and σ over the overlap period are summarized in Table 2.

Table 2

Mean the Median and 68% Confidence Interval σ of the Collocated Missions over a Paring Time Period

	$\overline{Median}$ (K) / $\bar{\sigma}$(K)		
Height layers (km)	COSMIC1-Metop	COSMIC2-Metop	SPIRE-Metop
	90ºS-90ºN (45ºS-45ºN for COSMIC-2)		
8-12	-0.01/0.95	0.05/0.83	-0.01/0.88
12-20	-0.02/0.98	0.03/0.94	0.02/0.97
20-30	-0.04/1.74	0.19/1.82	0.08/1.74
	60ºN-90ºN		
8-12	0.01/1.1	-	0.01/1.0
12-20	0.00/0.95	-	0.04/1.0
20-30	0.02/1.75	-	0.16/1.9
	20ºN-60ºN (20ºN-45ºN for COSMIC-2)		
8-12	-0.01/0.96	0.08/0.92	-0.01/0.90
12-20	-0.01/1.00	0.01/1.06	0.03/1.02
20-30	-0.05/1.7	0.25/1.86	0.14/1.75
	20ºS-20ºN		
8-12	-0.03/0.72	0.03/0.75	-0.01/0.67
12-20	-0.02/0.80	0.04/0.86	-0.02/0.80
20-30	-0.1/1.73	0.17/1.85	-0.09/1.67
	60ºS-20ºS (45ºS-20ºS for COSMIC-2)		
8-12	-0.03/0.97	0.08/0.88	-0.02/0.88
12-20	-0.05/1.01	0.02/0.99	0.01/0.98
20-30	-0.07/1.69	0.17/1.76	0.04/1.63
	90ºS-60ºS		
8-12	0.01/1.0	-	-0.02/0.96
12-20	0.03/1.04	-	0.02/1.03
20-30	0.03/1.91	-	0.13/1.90

Figure 4 shows that in the upper troposphere, COSMIC-1, COSMIC-2, and SPIRE are consistent with Metop at all latitude zones, except COSMIC-2, exhibiting a slight positive bias in SHSM and NHSM. The average bias is below 0.08 K, and σ increases from around 0.7 K at TRO to 1 K at SHP/NHP. The slight positive bias of COSMIC-2 in the midlatitudes may be caused by the observations with a side-looking view (view angle ranging from 60º to 120º) where the low antenna gain results in relatively small SNR. The impact of view angle on retrieval accuracy will be investigated in a separate study. All the missions agree very well with each other in tropopause and lower stratosphere (Figure 5). The average difference is below 0.05 K with σ around 1 K, which reflects measurement errors and atmospheric temperature variation within the match window.

The first impression in the mid-stratosphere (Figure 6) is that the variation of mission difference and σ are larger than those at the lower altitudes below. Compared to other mission pairs, COSMIC-1 is still consistent with Metop, with the average difference below 0.1 K and σ below 1.9K. SPIRE has a positive bias slightly larger than 0.1 K in NHP, NHSM, and SHP regions. As for COSMIC-2, obvious positive bias relative to Metop appears at all latitude zones from 45ºS to 45ºN. The average bias at NHSM and TRO/SHSM is 0.25 K and 0.17 K, respectively. A noteworthy feature is that the bias of COSMIC-2 at TRO and the σ of COSMIC-2 and SPIRE in TRO and mid-latitudes gradually increase with time, and the trend seems aligned with the 25th solar cycle. The impact of the residual ionospheric correction most likely causes the large bias and σ at this altitude region. The relatively large positive bias in COSMIC-2 indicates it might be more susceptible to ionospheric impact. This is consistent with what Mannucci et al. (2011) found in their study that LEO at lower altitudes tends to have higher residual ionospheric error due to the partial top and bottom side ionosphere cancellation and the violation of the assumption that refractive index is unity at the receiver. Additionally, since the profiles from different missions are collocated based on the latitude and longitude at the tangent point of 5 km, the paired profiles can be more than 150 km apart at higher altitudes, resulting in larger discrepancies among profiles at such heights. Overall, the mean mission differences are less than 0.1 K at all latitudes and heights below 20 km and increase with altitude. σ is around or below 1K below 20 km and increases to about 2K above 20 km. Such a pattern is consistent with what Hajj (2004) found when comparing CHAMP and SAC-C using a similar method.

The root cause of the relatively large positive bias in COSMIC-2 will be investigated in a separate study. The impact of the mission difference on temperature trend estimation is further examined through a sensitivity experiment in Section 5. It reveals that COSMIC-2 positive bias above 20 km can increase the temperature trend by 0.05 K/Decade, exceeding the GCOS required measurement stability. Therefore, in this study, COSMIC-2 data above 20 km are excluded from generating the multi-mission MMC.

4.2 Validation of the Sampling Error Correction

4.2.1 Sampling Error Features

This section investigates the systematic behavior of the sampling errors of the Sun-synchronous and non-Sun-synchronous satellites. COSMIC-1 and Metop-A are taken as examples. The sampling error of these two satellites from 2009 to 2012 is first estimated by using the method described in Section 3.3 and then averaged in TRO, NHSM, and NHP to give the temporal evolution of region-average sampling errors for the entire four years. The result is presented in Figure 7.

As illustrated in Figure 7 (a)-(b), the sampling error caused by local time coverage is well discernible in the tropics. With a drifting orbit that can cover the entire diurnal cycle of atmospheric temperature within one month, COSMIC-1's sampling error is characterized by quasi-random positive and negative deviation within ±0.05 K. The bias is as low as -0.003 K. Before 2017, Metop-A has a Sun-synchronous orbit with a fixed ECT, resulting in limited local time coverage (see Figure 1 (c)). Such skew-symmetric sampling of the temperature diurnal cycle leads to a small positive bias (0.03 K on average) compared to the full local time sampling. Such systematic bias can be expected to be persistent over the lifetime of a Sun-synchronous satellite with a fixed ECT.

The sampling error in the NHSM region (Figure 7 (c)-(d)) has a visible band at altitudes from about 12 to 20 km. This band persists almost during the whole observation period for both COSMIC-1 and Metop-A. Such an increase in sampling error (above 0.2 K) is caused by the comparatively larger temperature variability around the tropopause over subtropics and midlatitudes, which the limited spatiotemporal coverage RO observations cannot fully capture.

The large sampling errors around the NPH region caused by the wintertime polar vortex shown in Figure 3 (c) are also recognizable in Figure 7 (e)-(f). The highest sampling error is found in January 2010, -1.7 K for COSMIC-1 and -3.4 K for Metop-A, associated with the exceptionally cold polar vortex in mid-winter followed by a major sudden stratospheric warming occurring near the end of January (Dörnbrack et al. 2012).

It is noted that the local time component of sampling error diminishes at higher latitudes. This is because temperature variability at higher latitudes is stronger than at the tropics, which exceeds the impact of local time coverage. In addition, satellite orbit geometry allows measurements to spread at a broader local time range at higher latitudes, resulting in a smaller local time component in sampling error. The sampling error features exhibited in this section are consistent with those found in previous studies (Pirscher et al. 2007; Shen et al. 2021). The evident sampling errors in MMC_{obs} and their distinct patterns among different missions demonstrate the necessity of sampling error correction.

4.2.2 RO Mission Difference before and after Correction

Figure 8 depicts the difference between COSMIC-1 and Metop-A MMC in January 2009 before and after sampling error correction. To assess the impact of reanalysis models on sampling error estimates, three models, MERRA-2, JRA-55, and ERA-5, are employed to experiment. The large MMC difference at the high northern latitude caused by the wintertime polar vortex is pronounced in MMC_{obs} in Figure 8 (a). The mission deviation can be as high as 6.6 K in the stratosphere of the North Pole. After sampling error correction, this negative bias is largely eliminated in MMC_{crr} as shown in Figure 8 (b)-(d), keeping the mission difference below 1 K.

The sampling error corrected results show that the mission difference is slightly larger above 20 km over the equatorial regions and high latitudes than the rest. This is because the sharp temperature change due to Quasi-Biennial Oscillation (QBO) and winter polar vortex, and the poor RO coverage at high latitudes lead to large sampling errors that cannot be completely removed by the reanalysis models with limited spatiotemporal resolution. Besides the residual sampling error, the difference in instrumental noise, signal-tracking methods, and accuracy among missions also contributes to the deviation remaining in MMC_{crr} (Scherllin-Pirscher et al. 2011; Gleisner et al. 2020). Comparison of Figure 8 (b)-(d) shows that different reanalysis models result in similar MMC_{crr}. The impact of reanalysis models on sampling error correction and temperature trend estimates will be further quantified in Section 4.2.3.

Figure 9 presents the monthly bias and standard deviation of the MMC mission differences during their overlap observation period. The black and red lines with the error bar represent the statistics before and after sampling error correction by ERA-5. The image shows that the correction significantly decreases the bias and standard deviation of the MMC difference between missions. Specifically, after sampling error correction, the mean/standard deviation of the MMC difference between Metop and COSMIC-1 is reduced from 0.06 K/0.46 K to 0.05K/0.19 K. For Metop and SPIRE, the mean/standard deviation of the MMC difference is reduced from -0.02 K/0.5 K to -0.007 K/0.2 K. Figure 9 (a) also shows that the standard deviation of the difference between the raw Metop and COSMIC-1 data has been gradually increasing since 2015. This is caused by the continuous decline of the COSMIC-1 observation number, as shown in Figure 1 (a). This pattern is not obvious for sampling error-corrected results until the end of 2018.

The experiment in this section demonstrates that different sampling errors caused by different spatiotemporal sampling characteristics among satellites are the primary cause of the mission difference in MMC. The correction method described in Section 3.3 can effectively reduce sampling errors and thus reduce the mission difference in MMC.

4.2.3 Uncertainty in Sampling Error Correction

To quantify the uncertainty in sampling error correction caused by reanalysis models and its impact on temperature trend estimates, three different models, ERA-5, JRA-55, and MERRA-2, are employed in sampling error correction for the MMC generated from combined missions from September 2006 to July 2023. The result is presented in Figure 10.

Figure 10 (a) shows the global monthly average of the difference between MMC_{Int} and MMC_{obs} calculated through Equation (1). MMC_{Int} is obtained by subsampling three reanalysis model fields. The difference between MMC_{Int} and MMC_{obs} and the difference among individual MMC_{Int} are notable. The overall average deviation of MMC_{Int} from MMC_{obs} is 0.16 K, 0.12 K, and 0.20 K for ERA-5, JRA-55, and MERRA-2, respectively. This indicates that the temperature profiles provided by reanalysis models and observed by GNSS RO significantly differ.

Figure 10 (b) illustrates the global monthly average of sampling errors estimated by reanalysis models through Equation (1)-(3). It shows that the sampling errors quantified from different reanalysis models are consistent. They all exhibit obvious seasonal variations associated with seasonal cycles in atmospheric temperature. The overall averaged difference between the sampling error estimated by JRA-55 and ERA-5 is 0.003 K, and the difference between the sampling error estimated by MERRA-2 and ERA-5 is 0.002 K, much smaller than the difference in the modeled temperature fields shown in Figure 10 (a). This is consistent with what is shown in Figure 8. A slightly higher difference is found in the northern and southern hemispheres during wintertime. This is caused by the large temperature change in the polar vortex, which cannot be accurately detailed in reanalysis models with limited spatial and temporal resolution.

Figure 10 (c) presents the global temperature anomalies and trends based on the MMC_{crr} calibrated by these three models through Equation (4). Anomalies are relative to a climatological seasonal cycle of MMC_{crr} from January 2007 to December 2022. The temperature trends and their uncertainties with 95% confidence intervals are listed at the bottom of the panel. It shows that the temperature anomalies and trends calculated from different model calibrated MMC_{crr} are almost identical to each other, all pointing to a nearly zero temperature trend in UTLS. The deviation in temperature trends caused by applying different models in sampling error correction is below 0.001 K/Dec, much lower than the measurement stability required by the Global Climate Observing System (GCOS), 0.05 K/Decade (GCOS, 2016). The slight difference in sampling error does not impact temperature anomalies and trends attributable to deseasonalization.

This experiment demonstrates that the inconsistency in atmospheric states among various models has little impact on sampling error estimation and, thus, the estimate of anomalies and trends. This is because the accuracy of the estimated sampling error depends on how accurately the model can capture the true atmospheric variability within the monthly latitude bins. The model state's absolute accuracy is unimportant since it has already been largely removed by the subtraction in Equation (3).

4.3 Comparison of Temperature Anomaly with ROMSAF

In this section, the time-dependent temperature anomalies calculated from STAR ROPP MMC are compared to the anomalies based on ROM SAF MMC during their overlap period (September 2006-December 2016). The time series of anomaly difference (STAR ROPP minus ROM SAF) are computed at three vertical layers, including the upper troposphere (8-12 km), the lower stratosphere including tropopause (12-20 km), and the mid-stratosphere (20-30 km) at six latitude zones from Global, SHP, SHSM, TRO, NHSM, and NHP. The result is presented in Figure 11. The anomalies are calculated based on the climatological seasonal cycle from January 2007 to December 2016. The mean and standard deviation of the anomaly difference for all the regions are summarized in Table 3.

Table 3

Means and Standard Deviations of the Time Series of Temperature Anomaly Difference between STAR ROPP and ROM SAF

	Mean (K)/Standard deviation (K)		
	8-12 km	12-20 km	20-30 km
90ºS-90ºN	-0.001/0.02	-0.001/0.02	-0.002/0.05
60ºN-90ºN	0.000/0.03	-0.001/0.06	-0.006/0.25
20ºN-60ºN	0.000/0.02	0.000/0.03	0.003/0.08
20ºS-20ºN	-0.001/0.02	-0.001/0.03	-0.005/0.09
20ºS-60ºS	-0.001/0.03	-0.002/0.03	-0.001/0.08
60ºS-90ºS	-0.001/0.05	-0.002/0.09	-0.007/0.22

The anomaly difference between the two datasets shows no persistent bias. The average difference at all altitude and latitude zones is below 0.007 K, close to zero. However, the inter-monthly variance of anomaly difference varies dramatically among altitude layers and latitude regions. Two qualitative features can be inferred from Figure 11 and Table 3: (1) inter-monthly variance is smallest in the upper troposphere, larger in the lower stratosphere, and further increases above, and (2) within the same altitude layer, the variance tends to be larger at high latitudes than middle and low latitudes.

For example, the mid-stratosphere exhibits prominent anomaly variance (Figure 11 (a)), especially in SHP and NHP, where the standard deviation reaches 0.22 K and 0.25 K, respectively. The spikes observed in high latitude zones can be as high as 1 K in certain months and mostly coincide with the wintertime polar vortex. In altitude layers below the mid-stratosphere (Figure 11 (b)-(c)), the anomaly variance drops dramatically with a standard deviation well below 0.1 K. Spikes still occasionally occur in SHP and NHP, but the magnitude is below 0.4 K.

The larger anomaly deviation observed above 20 km is mostly attributable to the distinct bending angle initialization approaches implemented in the retrieval process at each GNSS RO research center. Bending angle background information is used in two parts of the RO retrieval chain. Firstly, when removing ionospheric contribution to the measured bending at an altitude above 50 km, where the signal-to-ratio is low, the measured L1/L2 bending angle data must be combined with a climatological bending angle profile to obtain optimal statistical results. Secondly, when deriving refractivity from bending angle data, the climatological bending angle profiles are used in the Abel integral to extend the corrected bending angle profiles above the highest measurement impact parameter. Although the background information is applied high above the stratosphere, its impact can propagate downward to lower altitudes for other derived parameters through the Abel integral. The inconsistency declines with decreasing altitudes, as the dependency of refractivity retrieval on bending angle background information weakens at lower altitudes.

The relatively larger variance appearing at high latitudes is mainly due to the residual sampling error. The strong temperature variability caused by the polar vortex and the poor RO coverage at high latitudes leads to large residual sampling errors in MMC and, thus, the large anomaly difference between the two datasets, as seen in Figure 8.

The lowest mean and standard deviation of anomaly difference is found in the tropical troposphere. Different RO mission combinations and the different configurations in the ROPP program between STAR RO DSC and ROM SAF could cause this slight anomaly deviation.

Overall, the anomaly difference between STAR ROPP and ROM SAF has no obvious bias, though the standard deviation is larger in the mid-stratosphere and high-latitude region. The anomaly variance is well below 0.1K except in the mid-stratosphere of polar areas. These features are consistent with previous studies (Ho et al. 2009; Steiner et al. 2020a) where the anomalies of various atmospheric parameters produced by multiple GNSS RO research centers were intercompared.

4.4 Comparison of Temperature Trend with ERA-5, MERRA-2, and JRA-55 Reanalysis

In this section, we derive the temperature trends in UTLS covering a period of 2006 to 2023 from the STAR-ROPP MMC and compare them with the trends generated from the ERA-5, JRA-55, and MERRA-2 reanalysis datasets to provide a better understanding of the time evolution of the STAR-ROPP MMC and its capability of monitoring climate signals. It should be noted that because of the lack of high-quality and high vertical resolution temperature observations and also the low vertical resolution of the model, the reanalysis data in the UTLS might be problematic (Zhao and Li, 2006; Trenberth and Smith, 2006, 2009; Shangguan et al. 2019). Evaluating the reanalysis datasets for their representation of temperature in the UTLS has become part of the goal of the Stratosphere-troposphere Processes And their Role in Climate (SPARC) Reanalysis Intercomparison Project (S-RIP) (Shangguan et al., 2019).

The MMC of the reanalysis data is constructed through Equation (2). The time series of temperature anomalies based on reanalyses and STAR-ROPP MMC are calculated for their overlap period of September 2006-April 2023 at three altitude layers and six latitude zones defined in Section 4.1. The climatological seasonal cycle used to obtain the anomalies is calculated by averaging MMC from 2007 to 2022. The temperature anomaly time series and their linear trends are presented in Figure 12-14, and the numbers are summarized in Table 4.

Table 4

Differences in the Temperature Trends Obtained from STAR-ROPP, ERA-5, JRA-55, and MERRA-2 for Six Latitude Zones and at Three Vertical Layers.

	Trend difference (K/Decade)		
Height layers (km)	STAR-ERA5	STAR-JRA	STAR-MERRA
	90ºS-90ºN		
8-12	-0.027*	-0.015*	0.000*
12-20	0.003*	0.008*	0.031*
20-30	0.064*	0.104*	0.002*
	60ºN-90ºN		
8-12	-0.067	0.027	-0.027
12-20	-0.006	0.012	0.010
20-30	0.117	0.150	0.097
	20ºN-60ºN		
8-12	-0.016*	-0.009*	-0.012*
12-20	-0.012	-0.005	0.015
20-30	0.043*	0.094*	0.006*
	20ºS-20ºN		
8-12	-0.035*	-0.046*	-0.011*
12-20	0.032*	0.022*	0.060*
20-30	0.105	0.157	0.002
	60ºS-20ºS		
8-12	-0.002*	0.005*	0.031*
12-20	-0.015*	0.004*	0.020*
20-30	0.023*	0.052*	-0.022*
	90ºS-60ºS		
8-12	-0.084	-0.002	0.004
12-20	-0.006	-0.005	0.002
20-30	0.039	0.028	-0.007

Note. The Trend Difference is Marked with an Asterisk when both Trends in Comparison are Significant at the 95% level.

Figure 12 shows the monthly temperature anomalies in the upper troposphere. STAR-ROPP exhibits good agreement with the three reanalyses in sub-seasonal variation of temperature anomalies and trends. All datasets point to significant positive trends in tropical and mid-latitudes and insignificant negative trends at high latitudes. The differences between the trends estimated by STAR-ROPP and reanalyses are less than 0.05 K/Decade at most latitude zones except at high latitudes where STAR-ROPP trends are lower than ERA-5 by about 0.08 K/Decade. The trend differences among reanalyses reach up to 0.09 K/Decade at high latitudes, slightly larger than the difference between STAR-ROPP and reanalyses. In the TRO (Figure 12 (d)), the temperature anomalies reveal clear interannual variation related to El Niño–Southern Oscillation (ENSO). Based on the Ocean Niño Index provided by NOAA (https://origin.cpc.ncep.noaa.gov/products/analysis_monitoring/ensostuff/ONI_v5.php), the pronounced warm anomalies found from November 2009 to February 2010 and from June 2015 to April 2016 are concurrent with the extensive outbreak of El Niño, while the large negative anomalies found from October 2007 to March 2008 and from August 2010 to January 2011 coincide with the strong La Niña events.

Figure 13 shows the temperature anomalies in the lower stratosphere. This is a transition layer between the upper-troposphere and mid-stratosphere where temperature has a complex variability structure. Nonetheless, the STAR-ROPP and all the three reanalyses agree very well on temperature anomalies and trends. They all exhibit positive trends in tropic and mid-latitude zones and negative trends in high-latitude areas. The trend difference between STAR-ROPP and reanalyses is below 0.06 K/Decade, comparable to the trend difference among three reanalyses.

The monthly zonal anomalies in the mid-stratosphere are presented in Figure 14. The strong inter-seasonal and interannual variations observed at SHP/NHP and TRO are related to polar vortex and QBO. The variation pattern of STAR-ROPP and reanalysis temperature anomalies are consistent with each other but with a relatively larger deviation in magnitude compared to altitudes below. The anomaly difference between STAR-ROPP and reanalyses can be as high as 0.5 K at tropic and 1.7 K at high latitudes. All data sets exhibit negative trends at all six latitude zones. STAR-ROPP's negative trends are weaker than ERA-5 and JRA-55 and closer to MERRA-2. The largest trend differences are found between STAR-ROPP and JRA-55 in TRO, reaching up to 0.16 K/Decade, while the trend difference between STAR-ROPP and MERRA-2 in this area is only 0.002 K/Decade. The trend difference among the three reanalyses also reaches up to 0.16 K/Decade in TRO.

The relatively larger anomaly difference observed at this altitude is caused by the same factor that leads to the STAR-ROPP and ROM SAF anomaly difference shown in Figure 11 (a). ERA-5 and MERRA-2 assimilate bending angles reprocessed by UCAR and NCAR/NCEP, respectively (Hersbach et al. 2020, Gelaro et al. 2017), while JRA-55 assimilates refractivities reprocessed by UCAR (Kobayashi et al. 2015). In the GNSS-RO retrieval chain, the use of climatological bending angle profiles alleviates the ionospheric contribution in bending angles above 50 km and initializes the Abel integral above the highest impact parameter. STAR-ROPP, UCAR, and NCAR/NCEP use different strategies and climate models to provide such background information. The impact of the different background information can propagate downward to lower altitudes through the Abel integral, resulting in larger anomaly deviation between reanalyses and STAR-ROPP in the mid-stratosphere. For the relatively short period of analysis, the larger difference in temperature anomaly, in turn, renders a somewhat larger deviation in temperature trends. Among all the three reanalyses, JRA-55 shows the largest deviation from STAR-ROPP at most latitudes. This is because JRA-55 assimilates refractivity, which is further impacted by the climatological profiles used to initialize the Abel integral. Assimilating bending angles instead of the downstream product refractivities can mitigate the temperature discrepancy among the GNSS-RO and reanalysis datasets in the stratosphere.

Comparison of temperature anomalies from the troposphere to stratosphere at NHP/SHP (Figure 12-14 (b)/(f)) shows that the anomaly time series shares a similar pattern at those three height layers, but the magnitude decreases with decreasing altitude. This demonstrates that the polar vortex is the primary factor that causes the interannual change in temperature anomaly in high latitudes, and its impact declines from the stratosphere to the troposphere. This is consistent with Figure 3(c), where the large sampling error at NHP resulting from the polar vortex decreases with decreasing altitude.

A comparison of Figures 12 (d) and 14 (d) illustrates that positive ENSO is associated with warm temperature in the tropical upper troposphere and cold temperature anomalies in the stratosphere.

STAR-ROPP and all three reanalyses share this pattern, which is consistent with previous studies (Randel and Wu, 2015; Shangguan et al., 2019).

Globally, the temperature trends from STAR-ROPP show a robust cooling of -0.281 ± 0.044 K/Decade in the mid-stratosphere (20-30 km), coupling with a robust warming of 0.309 ± 0.085 K/Decade in the upper troposphere (8-12 km). According to a previous study (Shangguan et al. 2019), the warming temperature trends in the troposphere are mostly caused by the influence of sea surface temperature (SST), while the negative temperature trends in the stratosphere are primarily related to the radiative effects from the greenhouse gases (GHGs) and ozone-depleting substances (ODSs).

Figure 15 presents the vertical profiles of temperature trends with 0.2 km intervals estimated from STAR-ROPP, ERA-5, JRA-55, and MERRA-2 datasets. This overviews upper-air temperature trends from the lower troposphere to the mid-stratosphere for global and tropical coverages. As shown in Figure 15(a), STAR-ROPP shows global warming up to 0.35 K/Decade in the upper troposphere, followed by a notable decrease above 10 km. The warming trend remains constant around 0.22 K/Decade up to 16 km and then quickly changes from positive to negative (-0.34 K/Decade) around 25 km, from where it further slowly decreases to -0.43 K/Decade at 30 km. The temperature trends of the three reanalyses follow a similar pattern to that of STAR-ROPP at most altitudes, except above 25 km, MERRA-2 continues to decrease sharply to -0.65 K/Decade at 30 km. For the reanalysis and STAR-ROPP data sets, the trend uncertainty at a 95% confidence level ranges from 0.05 to 0.11 K/Decade. In the lower stratosphere, including tropopause (10-20 km), where temperature has a complex variability structure, the temperature trends estimated by ERA-5 are closest to STAR-ROPP among all the reanalyses. The trend difference between ERA-5 and STAR-ROPP is less than 0.03 K/Decade in this region, whereas the difference between the other two reanalyses and STAR-ROPP is up to 0.07 K/Decade for JRA-55 and 0.1 K/Decade for MERRA-2.

In the TRO (Figure 15 (b)), STAR-ROPP shows the warm trend first increases from 0.26 K/Decade to 0.48 K/Decade around 12 km and then gradually decreases to 0.29 K/Decade around 17 km from where it oscillates around 0.3 K/Decade till 21 km. In the mid-stratosphere, the positive trend decreases quickly into negative around 25 km and further decreases to -0.411

K/Decade at 30 km. The temperature trends from the reanalyses generally follow the STAR-ROPP at all altitudes. However, the difference between STAR-ROPP and reanalyses is larger than that in the global region. Around tropopause and lower stratosphere (17-20 km), where temperature exhibits strong vertical gradients, the ERA-5 trend is still closer to STAR-ROPP than other reanalyses with a difference of less than 0.03 K/Decade. The trend uncertainty at a 95% confidence level in TRO is much larger than that in the global zone. For the reanalysis and STAR-ROPP datasets, the trend uncertainty ranges from 0.11 to 0.2 K/Decade below 17 km and quickly increases from 0.2 to 0.35 K/Decade above 17 km.

A notable difference between Figure 15 (a) and 15 (b) is that the tropical trend has much higher uncertainty than the global trend. This is because of the large interannual temperature variation related to QBO and ENSO. The global and tropical temperature trends also share some common features. Below 10 km, STAR-ROPP shows a warming trend slightly smaller than the reanalyses, especially in the TRO. Considering that the STAR-ROPP dry temperature is compared with the reanalysis atmospheric temperature, the relatively higher water vapor content in the tropical upper troposphere is most likely responsible for this slight increment in trend deviation. Above 20 km, the deviation among STAR-ROPP and reanalyses grows larger than the altitudes below, mainly due to the impact of the bending angle background information. Trends vary similarly in the lower stratosphere, including tropopause, among STAR-ROPP and reanalyses. However, the reanalysis trends show an obvious stepwise pattern with abrupt changes around 15, 17, 19, and 21 km in both global and TRO regions, which is caused by the limit of the low vertical resolution of the reanalysis models. Compared to reanalyses, the temperature trends from STAR-ROPP exhibit a much more continuous and smooth variation with more details. With the high vertical resolution, typically about 100m in the troposphere and tropopause and about 1 km in the stratosphere (Steiner et al. 2020a), GNSS-RO has the unique capability of detailing the intricate temperature structure in the UTLS region.

The general pattern of the temperature trends showed in Figure 15 (a)-(b) is consistent with the near-global (70ºS-70ºN) and tropical upper-air temperature trends from 2002-2018 estimated by various data sets of GNSS RO, radiosondes, and microwave sounders in Steiner et al. (2020b). The fact that ERA-5 shows better agreement with RO observations in the UTLS region is aligned with Shangguan et al.'s study (2019), in which GNSS-RO was used as a reference to evaluate multiple reanalysis datasets. The prominent tropospheric warming and a transition to stratospheric cooling are consistent with the well-understood response of the UTLS region to long-term global warming.

The temperature trend for each latitude-altitude bin based on STAR-ROPP and reanalysis datasets is summarized in Figure 16. The lapse rate tropopause height is calculated from the MMC of the data sets following the World Meteorological Organization's (WMO) definition (WMO, 1957). The average tropopause heights throughout the analysis are marked as a gray line in Figure 16.

From the STAR-ROPP dataset, positive trends of 0.2-0.4 K/Decade are significant in most areas of the upper troposphere, with stronger warming up to 0.5-0.6 K/Decade in the northern hemisphere. Meanwhile, negative trends of 0.1-0.3 K/Decade dominate the mid-stratosphere. The warming extends through tropopause into the lower stratosphere from the tropics to the southern mid-latitudes. The atmosphere is cooling above the tropopause in the northern mid-latitudes, particularly in sub-tropical regions at 20 km. These features are consistent with previous studies (Shangguan et al. 2019; Gleisner et al. 2022; Ladstädter et al. 2023).

Reanalyses show good agreement with the STAR-ROPP regarding the general pattern of temperature trends. However, slight differences can be found among datasets. JRA-55 has relatively warmer trends in the TRO around 12-15 km and colder trends in the NHSM above 25 km. Around the tropical tropopause, where other datasets exhibit neural trends, JRA-55 shows slightly insignificant positive trends (0.1-0.2 K/Decade). The cooling trends centered in the NPH around 15 km and the south hemisphere above 25 km appear weaker in MERRA-2 than in the other datasets. Compared to STAR-ROPP, all three reanalyses show fewer details and abrupt changes in temperature trends around tropical tropopause due to their limited vertical resolution. Overall, ERA-5 shows the best agreement with STAR-ROPP with a similar pattern and comparable magnitude of temperature trends at most altitude and latitude regions.

An insignificant warming signal is observed in all datasets around 20-25 km in the tropics, which has not been found in previous studies (Shangguan et al. 2019; Gleisner et al. 2022; Ladstädter et al. 2023). For a relatively short period, this warming trend is most likely related to the decadal-scale variability in the QBO-associated temperature anomalies in the stratosphere (e.g., Martin et al. 2021). The multiple linear regression method was adopted to assess and limit the impact of ENSO and QBO on long-term trends in past studies (Shangguan et al. 2019; Gleisner et al. 2022; Ladstädter et al. 2023). As a preliminary work, this study will not estimate the effects from both ENSO and QBO because of the relatively short data record. However, further exploration is warranted, especially when the relatively longer data record becomes available in the future.

5 Discussion

Section 4.1 shows that relative to Metop, COSMIC-2 has a slight positive bias (0.08 K) outside of 20ºS-20ºN in the upper troposphere and 0.17-0.25 K positive bias at all latitude zones from 45ºS-45ºN in the mid-stratosphere. In this section, a sensitive experiment is carried out to assess the impact of the COSMIC-2 bias on the temperature trend estimation. The temperature anomalies and trends are calculated based on all RO missions and all missions excluding COSMIC-2 data at altitude regions 8-12 km and 20-30 km and latitude zone from 60ºS-60ºN. ERA-5 temperature anomaly and trend are also listed for comparison. The results are presented in Figures 17-18.

Figures 17 (b) and (d) illustrate that the slight positive bias of COSMIC-2 in midlatitudes increases the estimated temperature trend by about 0.02 K/Decade, well below the GCOS required measurement stability. Figures 17 (a) and (c) show that the difference in temperature trend caused by COSMIC-2 bias in TRO and the global zone is even smaller. Thus, the impact of COSMIC-2 slight positive bias in the upper troposphere can be neglected.

Figure 18 demonstrates that since October 2019, when the COSMIC-2 mission began, the temperature anomalies estimated from all missions are higher than those estimated from the missions without COSMIC-2. By removing the COSMIC-2 data, which has a relatively large positive bias compared to other missions, the estimated temperature trend declines by around 0.05 K/Decade for all latitude zones, making the trend closer to that derived from ERA-5.

Data consistency among missions is essential to produce reliable RO climatology. Before finding a solution to the issue of its positive bias above 20 km, COSMIC-2 data is excluded in the construction of STAR-ROPP MMC above 20 km in this study. We will further investigate the possible reasons and find a solution to resolve the inconsistency caused by including the COSMIC-2 data.

6 Conclusions

This study focuses on constructing and evaluating the temperature climate data records in the upper troposphere and lower stratosphere (UTLS) based on the dry profiles produced by the GNSS RO science and data center at NOAA STAR (STAR RO DSC). Using UCAR low-level data as an input, the Radio Occultation Processing Package (ROPP) reconfigured by STAR RO DSC consistently generates RO bending angle, refractivity, and dry temperature profiles for multiple RO missions, including COSMIC-1, COSMIC-2, Metop (Metop-A/B/C), and SPIRE, which compose the STAR-ROPP dataset. We compare the collocated profiles from multiple STAR-ROPP processed RO missions to ensure data consistency. Based on this dataset, the temperature monthly mean climatology (MMC) is constructed on 2D latitude-height grids with a resolution of 5º in latitude by 0.2 km in height from 8-30 km, covering the period from April 2006 to July 2023. The sampling error in MMC is corrected by using ERA-5 reanalysis. The uncertainty of the sampling error correction method is quantified through three different reanalysis models: ERA-5, MERRA-2, and JRA-55. The STAR-ROPP MMC is then evaluated by comparing it with the ROM SAF MMC and the MMC derived from the ERA-5, MERRA-2, and JRA-55 reanalysis datasets. We reach the following conclusions based on our analysis.

1. The comparison of the collocated dry temperature profiles from multiple missions shows good agreement in the upper troposphere and lower stratosphere, with mission differences well below 0.1 K. In the mid-stratosphere, COSMIC-1 still exhibits good consistency with Metop. At the same time, SPIRE shows a slight positive bias up to 0.16 K in polar areas, and COSMIC-2 has a larger positive bias ranging from 0.17-0.25 K, with the evident increasing trend in the tropics seemingly coherent with the 25th solar cycle. The impact of the residual ionospheric correction most likely causes a relatively large bias and standard deviation at this altitude. A sensitivity study shows that the COSMIC-2 positive bias in the mid-stratosphere can increase the temperature trend by about 0.05 K/Decade in this region. Therefore, in this study, COSMIC-2 data above 20 km has been excluded from the construction of STAR-ROPP MMC.

2. The sampling error correction method can correctly identify and effectively reduce the sampling error in MMC. It reveals the distinct sampling error features of the Sun-synchronous and non-Sun-synchronous satellites in the tropical region. The large sampling errors caused by the sharp temperature change at the tropopause and wintertime polar vortex at high latitudes are also identified. After applying the sampling error correction, the mission difference in MMC is largely removed: the bias and standard deviation of the MMC mission differences during their overlap period is reduced from 0.06 K/0.46 K to 0.05K/0.19 K for Metop and COSMIC-1, and from -0.02 K/0.5 K to -0.007 K /0.2 K for Metop and SPIRE. The uncertainty in the sampling error correction method is assessed by employing ERA-5, MERRA-2, and JRA-55. All three models yield similar sampling errors despite the relatively large discrepancy in their atmospheric states. The global UTLS temperature anomalies and trends derived from the MMC with sampling error corrected by the three models are almost identical. This suggests that the sampling error correction method is a robust approach unaffected by the model state's absolute accuracy.
3. Comparison of the temperature anomaly time series between STAR-ROPP and ROMSAF during their overlap period (September 2006-December 2016) exhibits good agreement. The mean and standard deviation of their anomaly difference are below 0.005 K and 0.1 K at all altitude and latitude zones except in the mid-stratosphere around polar regions. A relatively larger inter-monthly variance is found in the mid-stratosphere than in the altitudes below because STAR-ROPP and ROMSAF use different bending angle background information in their retrieval chain. A relatively larger deviation between the two datasets observed at high latitudes is mainly related to the residual sampling error. The sharp temperature change during the wintertime polar vortex and the poor RO coverage at this region lead to larger sampling errors that cannot completely be removed by reanalysis models with limited spatiotemporal resolution.
4. Generally, the temperature anomaly and trends estimated by STAR-ROPP agree well with those estimated from ERA-5, MERRA-2, and JRA-55 over 17 years (September 2006-April 2023). The difference in the temperature trends between STAR-ROPP and reanalyses is below 0.06 K/Decade in the UTLS region (8-20 km) except in polar areas where polar vortex and poor RO coverage result in residual sampling errors. Relatively larger trend differences are found in the mid-stratosphere (20-30 km) due to the impact of different bending angle

background information used in the retrieval chain of different GNSS-RO process centers. The trend difference between STAR-ROPP and reanalyses shows a slight increase below 10 km, especially in the tropics. This is due to the relatively high humidity in the tropical upper troposphere, which makes the approximation of physical temperature to dry temperature less accurate. Around tropopause, where the temperature has an intricately variable structure, ERA-5 has the best agreement with STAR-ROPP. However, all the reanalysis trends exhibit an apparent stepwise pattern due to their coarse vertical resolution. The fact that STAR-ROPP trends present a much more continuous and smooth variation with altitudes suggests that it has the unique capability of detailing the intricate temperature structure in the UTLS region.

5. STAR-ROPP MMC constructed in this study can identify various climate signals and monitor long-term climate change. For example, the interannual temperature variation related to Quasi-Biennial Oscillation (QBO) and El Niño–Southern Oscillation (ENSO) events are well represented by the STAR-ROPP temperature anomaly time series. The global temperature trends estimated by STAR-ROPP show a transition from a prominent warming of 0.309 ± 0.085 K/Decade in the upper troposphere (8-12 km) to a robust cooling of -0.281 ± 0.044 K/Decade in the mid-stratosphere (20-30 km). The warming in the troposphere extends through tropopause into the lower stratosphere from the tropics to the southern mid-latitude regions. These findings are consistent with previous studies and the well-understood response of the UTLS region to long-term global warming.

The larger mission difference found in the mid-stratosphere in STAR-ROPP datasets may lead to uncertainties in the temperature trend estimation in these regions. Its cause and possible solution are still under investigation. Relatively higher deviations between STAR-ROPP and other datasets, such as ROMSAF and various reanalyses, are found in the mid-stratosphere and high latitudes. Efforts are being made to reduce such deviation by implementing more accurate and consistent bending angle background information in the retrieval process and employing a high-resolution reanalysis model in the sampling correction method. Additionally, to alleviate the uncertainty in the trend estimation, multiple linear regression will be applied to diminish the inter-seasonal and interannual variability caused by natural phenomena, such as QBO and ENSO.

Figure 1. Statistics on the valid RO profiles used to generate STAR ROPP MMC. (a) Monthly mean daily number of valid profiles. (b) Latitude and (c) local time distribution of RO profiles in September 2009 of COSMIC-1 and Metop-A and September 2022 of COSMIC-2 and SPIRE. Here, Metop represents all the Metop-A/-B/-C observations.

Figure 2. Statistics on the collocated pairs. (a) Global distribution of COSMIC-2 (red dots) and Metop (green dots) pairs for May 2021. (b) The monthly number of COSMIC-1 (blue), COSMIC-2 (red), and SPIRE (green) profiles collocated with Metop.

Figure 3. Zonally gridded monthly mean of dry temperature from COSMIC-1 in January 2009 (a) before and (b) after sampling error correction. (c) sampling error estimated by ERA-5.

Figure 4. Measures of consistency between COSMIC-1 and Metop (blue), COSMIC-2 and Metop (red), and SPIRE and Metop pairs (green) at 8-12 km layer for (a) the entire globe (90ºS-90ºN), (b) NHP (60ºN-90ºN), (c) NHSM (20ºN-60ºN), (d) TRO (20ºS-20ºN), (e) SHSM (60ºS-20ºS), and (f) SHP (90ºS-60ºS).

Figure 5. Same as Figure 4, but for the 12-20km layer.

Figure 6. Same as Figure 4, but for the 20-30km layer.

Figure 7. Time series of monthly region-average temperature sampling error of (left) COSMIC-1 and (right) Metop-A for the (a-b) 20ºS-20ºN zone, (c-d) 20ºN-60ºN zone, (e-f) 60ºN-90ºN zone.

Figure 8. Differences of Metop-A and COSMIC-1 zonally gridded monthly mean of dry temperature in January 2009 (Metop-A minus COSMIC-1). (a) before sampling error correction and after sampling error corrected by (b) MERRA-2, (c) JRA-55, and (d) ERA-5.

Figure 9. Time series of the mean and standard deviation of the MMC difference between missions. (a) MMC difference between Metop and COSMIC-1, and (b) MMC difference between Metop and SPIRE. Black and red lines with error bars represent the difference before and after sampling error correction by ERA-5.

Figure 10. Time series of the monthly average of (a) MMC_{Int} relative to MMC_{obs}, (b) the estimated sampling errors, and (c) temperature anomalies and trends for the global UTLS region.

Different colors represent the results from different reanalysis models. The temperature trends and their uncertainties with 95% confidence intervals are listed below (c).

Figure 11. Time series of the temperature anomaly difference between STAR ROPP and ROM SAF (STAR ROPP minus ROM SAF) at 20-30 km (a), 12-20 km (b), and 8-12 km (c) for six latitude zones represented by different color lines.

Figure 12. Temperature anomalies (solid line) of STAR-ROPP (red), ERA-5 (black), JRA-55 (blue), and MERRA-2 (green) at 8-12 km layer for (a) the entire globe (90^{o}S-90^{o}N), (b) NHP (60^{o}N-90^{o}N), (c) NHSM (20^{o}N-60^{o}N), (d) TRO (20^{o}S-20^{o}N), (e) SHSM (60^{o}S-20^{o}S), and (f) SHP (90^{o}S-60^{o}S). Overplotted are their corresponding linear trends (dashed line). The trend and its uncertainty at a 95% confidence level are listed on each panel. Trends significant at the 95% level are marked with asterisks.

Figure 13. Same as Figure 12, but for the 12-20 km layer.

Figure 14. Same as Figure 12, but for the 20-30 km layer.

Figure 15. Vertically resolved temperature trends 2006-2023 estimated from STAR-ROPP (red), ERA-5 (black), JRA-55 (blue), and MERRA-2 (green) for (a) global (90^{o}S-90^{o}N) and (b) the TRO (20^{o}S-20^{o}N) regions. Error bars represent the trend uncertainty at the 95% confidence level.

Figure 16. Altitude vs. latitude resolved temperature trends for (a) STAR-ROPP, (b) ERA-5, (c) JRA-55, and (d) MERRA-2. The gray lines mark the average tropopause height calculated with STAR-ROPP and reanalysis MMC. Areas with trends significant at the 95% confidence level are indicated with dots.

Figure 17. Temperature anomalies (solid line) estimated from all missions (red) and missions excluding COSMIC-2 (green) and ERA-5 (blue) at 8-12 km layer for (a) the entire globe (90^{o}S-90^{o}N), (b) NHSM (20^{o}N-60^{o}N), (d) TRO (20^{o}S-20^{o}N), (e) SHSM (60^{o}S-20^{o}S). Overplotted are their corresponding linear trends (dashed line). The trend and its uncertainty at a 95% confidence level are listed on each panel.

Figure 18. The same as Figure 17 but for 20-30 km.

Acknowledgments

This study was supported by NOAA grant NA19NES4320002 (Cooperative Institute for Satellite Earth System Studies -CISESS) at the University of Maryland/ESSIC. The scientific results and conclusions, as well as any views or opinions expressed herein, are those of the authors and do not necessarily reflect those of NOAA or the Department of Commerce.

Data Availability Statement

The STAR SDC processed dry temperature profiles from multiple GNSS RO missions are publicly available from the NOAA/STAR website: https://gpsmet.umd.edu/star_gnssro/description.html. ROM SAF MMC dataset is publicly available at: https://preop.romsaf.org/product_archive.php. ERA-5 data is publicly available at: https://cds.climate.copernicus.eu/cdsapp#!/dataset/reanalysis-era5-pressure-levels?tab=overview. MERRA-2 data is publicly available at https://daac.gsfc.nasa.gov/. JRA-55 data is publicly available at https://jra.kishou.go.jp/JRA-3Q/index_en.html. Ocean Niño Index is publicly available at: https://origin.cpc.ncep.noaa.gov/products/analysis_monitoring/ensostuff/ONI_v5.php

References

Anthes, R. A. (2011). Exploring Earth's atmosphere with radio occultation: contributions to weather, climate and space weather. *Atmospheric Measurement Techniques*, 4 (6), 1077–1103. https://doi.org/10.5194/amt-4-1077-2011.

Ball, W. T., Alsing, J., Mortlock, D. J., Staehelin, J., Haigh, J. D., Peter, T. et al. (2018). Evidence for a continuous decline in lower stratospheric ozone offsetting ozone layer recovery. *Atmospheric Chemistry and Physics*, 18 (2), 1379–1394. https:// doi. org/ 10. 5194/ acp- 18- 1379- 2018.

Birner, T. & Charlesworth, E. J. (2017). On the relative importance of radiative and dynamical heating for tropical tropopause temperatures. *Journal of Geophysical Research: Atmospheres*, 122 (13), 6782–6797. https:// doi. org/ 10. 1002/ 2016J D0264 45.

Cardinali, C. & Healy, S. (2014). Impact of GPS radio occultation measurements in the ECMWF system using adjoint based diagnostics, *Quarterly Journal of the Royal Meteorological Society*, 140 (684), 2315–2320. https://doi.org/10.1002/qj.2300.

Charlesworth, E. J., Birner, T. & Albers, J. R. (2019). Ozone transport-radiation feedbacks in the tropical tropopause layer. *Geophysical Research Letters*, 46 (23), 14195–14202. https://doi.org/10.1029/2019GL084679

Dach R., Lutz S., Walser P., & Fridez P. (2015), Bernese GNSS Software Version 5.2, Astronomical Institute, UniversityofBern. chrome-extension://efaidnbmnnnibpcajpcglclefindmkaj/http://www.bernese.unibe.ch/docs/DOCU52.pdf

Dörnbrack, A., Pitts, M. C., Poole, L. R., Orsolini, Y. J., Nishii, K., & Nakamura, H. (2012). The 2009–2010 Arctic stratospheric winter – general evolution, mountain waves and predictability of an operational weather forecast model. *Atmospheric Chemistry and Physics*, 12 (8), 3659–3675. https://doi.org/10.5194/acp-12-3659-2012.

Eyring, V., Bony, S., Meehl, G. A., Senior, C. A., Stevens, B., Stouffer, R. J., & Taylor, K. E. (2016). Overview of the Coupled Model Intercomparison Project Phase 6 (CMIP6) experimental design and organization. *Geoscientific Model Development*, 9 (5), 1937–1958, https://doi.org/10.5194/gmd-9-1937-2016.

Fu, Q., Manabe S., & Johanson C. M. (2011). On the warming in the tropical upper troposphere: Models versus observations. *Geophysical Research Letters*, 38 (15), L15704, https://doi.org/10.1029/2011GL048101.

GCOS (2016): The global observing system for climate: implementation needs, GCOS-200, World Meteorological Organization, available at: https://library.wmo.int/doc_num.php?explnum_id=3417 (last access: 15 February 2024).

Gelaro, R., McCarty, W., Su´arez, M.J., Todling, R., Molod, A., Takacs, et al. (2017). The Modern-Era retrospective analysis for research and applications, version 2 (MERRA- 2). *Journal of Climate*, 30 (14), 5419–5454. https://doi.org/10.1175/JCLI-D-16-0758.1.

Gleisner, H. (2011). GRAS SAF Report 10: Latitudinal Binning and Area-Weighted Averaging of Irregularly Distributed Radio Occultation Data, Danish Meteorological Institute. Danish Meteorological Institute. chrome-extension://efaidnbmnnnibpcajpcglclefindmkaj/https://rom-saf.eumetsat.int/general-documents/gsr/gsr_10.pdf

Gleisner, H., Lauritsen, K. B., Nielsen, J. K. & Syndergaard, S. (2020). Evaluation of the 15-year ROM SAF monthly mean GPS radio occultation climate data record. *Atmospheric Measurement Techniques*. 13 (6), 3081–3098, https://doi.org/10.5194/amt-13-3081-2020.

Gleisner, H., Ringer, M. A. & Healy, S. B. (2022). Monitoring global climate change using GNSS radio occultation. *npj Climate and Atmospheric Science,* 5, 6. https://doi.org/10.1038/s41612-022-00229-7.

Haimberger, L., Tavolato C., & Sperka S. (2008). Toward eliminating the warm bias in historic radiosonde temperature records - Some new results from a comprehensive intercomparison of upper-air data. *Journal of Climate*, 21 (18), 4587–4606, https://doi.org/10.1175/2008JCLI1929.1.

Haimberger, L., Tavolato C., & Sperka S. (2012). Homogenization of the global radiosonde temperature dataset through combined comparison with reanalysis background series and neighboring stations. *Journal of Climate,* 25 (23), 8108–8131, https://doi.org/10.1175/JCLI-D-11-00668.1.

Hajj G. A., Ao C. O., Iijima B. A., Kuang D., Kursinski E. R., Mannucci A. J. et al. (2004). CHAMP and SAC-C atmospheric occultation results and intercomparisons. *Journal of Geophysical Research: Atmospheres*,109 (D6), https://doi.org/10.1029/2003JD003909

Healy, S. B., Jupp, A. M., & Marquardt, C. (2005). Forecast impact experiment with GPS radio occultation measurements. *Geophysical Research Letters*, 32 (3), L03804, https://doi.org/10.1029/2004GL020806

Hersbach, H., Bell B., Berrisford, P., Hirahara, S., et al. (2020). The ERA5 global reanalysis. *Quarterly Journal of the Royal Meteorological Society,* 146 (730), 1999–2049. https://doi.org/10.1002/qj.3803

Ho, S.-P., Kirchengast, G., Leroy, S., Wickert, J., Mannucci, A. J., Steiner, A. K. et al. (2009). Estimating the uncertainty of using GPS radio occultation data for climate monitoring: Intercomparison of CHAMP refractivity climate records for 2002 to 2006 from different data centers. *Journal of Geophysical Research: Atmospheres*, 114 (D23), D23107, https://doi.org/10.1029/2009JD011969.

Ho, S.-P., Anthes, R. A., Ao, C. O., Healy, S., Horanyi, A., Hunt, D., A. et al. (2019). The COSMIC/FORMOSAT-3 Radio Occultation Mission after 12 years: Accomplishments, Remaining Challenges, and Potential Impacts of COSMIC-2, *Bulletin of the American Meteorological Society*, 101 (7), E1107–E1136, https://doi.org/10.1175/BAMS-D-18-0290.1

Ho, S.-P., Pedatella, N., Foelsche, U., Healy, S., Weiss, J.-P., Ullman, R. (2022). Using Radio Occultation Data for Atmospheric Numerical Weather Prediction, Climate Sciences, and Ionospheric Studies and Initial Results from COSMIC-2, Commercial RO Data, and Recent RO Missions, *Bulletin of the American Meteorological Society, 103 (11)*, E2506–E2512, https://doi.org/10.1175/BAMS-D-22-0174.1

Khaykin, S. M., Funatsu, B. M. Hauchecorne, A. et al. (2017). Post-millennium changes in stratospheric temperature consistently resolved by GPS radio occultation and AMSU observations. Geophysical Research Letters, 44 (14), 7510–7518, https://doi.org/10.1002/2017GL074353

Kidston, J., Scaife, A., Hardiman, S. et al. (2015). Stratospheric influence on tropospheric jet streams, storm tracks and surface weather. *Nature Geoscience*, 8, 433–440. https://doi.org/10.1038/ngeo2424

Kobayashi, S., Ota, Y., Harada, Y., Ebita, A., Moriya, M., Onoda, H., et al. (2015). The JRA- 55 reanalysis: general specifications and basic characteristics. *Journal of the Meteorological Society of Japan. Ser. II*, 93 (1), 5–48. https://doi.org/10.2151/jmsj.2015-001.

Kursinski, E. R., Hajj G. A., Schofield, J. T., Linfield, R. P., & Hardy, K. R. (1997). Observing Earth's atmosphere with radio occultation measurements using the Global Positioning System. Journal of Geophysical Research: Atmospheres, 102 (D19), 23429–23465, https://doi.org/10.1029/97JD01569

Ladstädter, F., Steiner, A.K. & Gleisner, H. (2023). Resolving the 21st century temperature trends of the upper troposphere–lower stratosphere with satellite observations. *Scientific Reports* **13**, 1306. https://doi.org/10.1038/s41598-023-28222-x.

Leroy, S. S., Dykema, J. A., & Anderson, J. G. (2006). Climate benchmarking using GNSS occultation. Atmosphere and Climate, Springer, Berlin Heidelberg, pp 287–301.

Leroy, S. S., Ao, C. O. & Verkhoglyadova, O. P. (2018). Temperature trends and anomalies in modern satellite data: Infrared sounding and GPS radio occultation. *Journal of Geophysical Research: Atmospheres,* 123 (20), 11431–11444, https://doi.org/10.1029/2018JD028990

Mannucci, A. J., Ao, C. O., Pi, X., & Iijima, B. A. (2011). The impact of large scale ionospheric structure on radio occultation retrievals. *Atmospheric Measurement Techniques*., 4 (12), 2837–2850, https://doi.org/10.5194/amt-4-2837-2011

Martin, Z., Sobel, A., Butler, A., & Wang, S. (2021). Variability in QBO temperature anomalies on annual and decadal time scales. Journal of Climate, 34(2), 589–605. https://doi.org/10.1175/JCLI-D-20-0287.1

Mears, C. A., & Wentz, F. J. (2017). Satellite-derived lower-tropospheric atmospheric temperature dataset using an optimized adjustment for diurnal effects. *Journal of Climate*, 30 (19), 7695–7718, https://doi.org/10.1175/JCLI-D-16-0768.1.

Mitchell, D. M., Thorne, P. W., Stott, P. A., & Gray, L. J., (2013). Revisiting the controversial issue of tropical tropospheric temperature trends. Geophysical Research Letters, 40 (11), 2801–2806, https://doi.org/10.1002/grl.50465

Pirscher, B., Foelsche, U., Lackner, B. C., & Kirchengast, G. (2007). Local time influence in single-satellite radio occultation climatologies from sun synchronous and non-sun-synchronous satellites. *Journal of Geophysical Research: Atmospheres*, 112 (D11), D11119, https://doi.org/10.1029/2006JD007934

Poli, P., Healy, S., & Dee, D. P. (2010). Assimilation of Global Positioning System Radio Occultation data in the ECMWF ERAInterim reanalysis, *Quarterly Journal of the Royal Meteorological Society*, 136 (653), 1972–1990, https://doi.org/10.1002/qj.722

Randel, W. J. & Wu, F. (2015). Variability of zonal mean tropical temperatures derived from a decade of GPS radio occultation data. *Journal of the Atmospheric Sciences*, 72 (3), 1261–1275, https://doi.org/10.1175/JAS-D-14-0216.1

Rohli, R. V. & Vega, A. J. (2017). Climatology fourth edition, Jones & Bartlett Learning , pp 418.

ROM SAF level 3 ATBD (2021): EUMETSAT ROM SAF Algorithm Theoretical Baseline Document: Level 3 gridded data version 4.3, 18 October 2021, The ROM SAF Consortium, chrome-extension://efaidnbmnnnibpcajpcglclefindmkaj/https://preop.romsaf.org/product_documents/romsaf_atbd_grd.pd

ROM SAF ROPP (2021): EUMETSAT ROM SAF The Radio Occultation Processing Package (ROPP) Pre-processor Module User Guide, version 11.0, The ROM SAF Consortium, 2021, Ref:SAF/ROM/METO/UG/ROPP/004, chrome-extension://efaidnbmnnnibpcajpcglclefindmkaj/https://rom-saf.eumetsat.int/romsaf_ropp_ug_pp.pdf.

Santer, B. D., Solomon, S., Pallotta, G. et al. (2017). Comparing tropospheric warming in climate models and satellite data. Journal of Climate, 30 (1), 373–392, https://doi.org/10.1175/JCLI-D-16-0333.1

Scherllin-Pirscher, B., Kirchengast, G., Steiner, A. K., Kuo, Y.-H., & Foelsche, U. (2011). Quantifying uncertainty in climatological fields from GPS radio occultation: an empirical-analytical error model, *Atmospheric Measurement Techniques*, 4 (9), 2019–2034. https://doi.org/10.5194/amt-4-2019-2011

Schmidt, T., Wickert, J., & Haser, A. (2010). Variability of the upper troposphere and lower stratosphere observed with GPS radio occultation bending angles and temperatures. *Advances in Space Research*, 46 (2), 150–161. https://doi.org/10.1016/j.asr.2010.01.021

Shangguan, M., Wang, W., & Jin, S. (2019). Variability of temperature and ozone in the upper troposphere and lower stratosphere from multi-satellite observations and reanalysis data. Atmospheric Chemistry and Physics , 19 (10), 6659–6679. https://doi.org/10.5194/acp-19-6659-2019, 2019.

Shen, Z., Zhang, K., He, Q., Wan, M., Li, L. & Wu, S. (2021). Quest over the sampling error of COSMIC radio occultation temperature climatologies. *Journal of Atmospheric and Oceanic Technology*, 38 (3), 441–458. https://doi.org/10.1175/JTECH-D-19-0169.1

Solomon S., Rosenlof K. H., Portmann, R. W. et al. (2010). Contributions of stratospheric water vapor to decadal changes in the rate of global warming. Science, 327 (5970), 1219–1223. DOI: 10.1126/science.1182488

Spencer, R.W., Christy, J. R. & Braswell, W. D. (2017). UAH Version 6 global satellite temperature products: Methodology and results. Asia-Pacific Journal of Atmospheric Sciences, 53, 121–130, https://doi.org/10.1007/s13143-017-0010-y

STAR-ROPP version 1.0 ATBD: Algorithm Theoretical Basis Document Inversion of Bending Angle and Refractivity profiles STAR ROPP Version 1.0 (Based on the ROPP Version 10.0) chrome-extension://efaidnbmnnnibpcajpcglclefindmkaj/https://gpsmet.umd.edu/star_gnssro/img/ATBD_STAR_ROPP_final.pdf

Steiner A. K., Lackner B. C., Ladstädter F., Scherllin-Pirscher B., Foelsche U., & Kirchengast G. (2011). GPS radio occultation for climate monitoring and change detection, *Radio Science*, 46 (6), RS0D24, https://doi.org/10.1029/2010RS004614

Steiner, A. K., Hunt, D., Ho, S.-P., Kirchengast, G., Mannucci, A. J., Scherllin-Pirscher, B et al. (2013). Quantification of structural uncertainty in climate data records from GPS radio occultation, *Atmospheric Chemistry and Physics*, 13 (3), 1469–1484. https://doi.org/10.5194/acp-13-1469-2013

Steiner, A. K., Ladstädter, F., Ao, C. O., Gleisner, H., Ho, S.-P. et al. (2020). Consistency and structural uncertainty of multi-mission GPS radio occultation records, *Atmospheric Measurement Techniques*, 13 (5), 2547–2575, https://doi.org/10.5194/amt-13-2547-2020

Steiner, A. K., Ladstädter, F., Randel, W. J., Maycock, A. C., Fu, Q. et al. (2020). Observed temperature changes in the troposphere and stratosphere from 1979 to 2018, *Journal of Climate*, 33 (19), 8165-8194. https://doi.org/10.1175/JCLI-D-19-0998.1

Titchner, H. A., Thorne, P. W., McCarthy, M. P., Tett S. F. B., Haimberger, L., & Parker, D. E. (2009). Critically reassessing tropospheric temperature trends from radiosondes using realistic validation experiments. *Journal of Climate*, 22 (3), 465–485, https://doi.org/10.1175/2008JCLI2419.1.

Trenberth, K. E. & Smith, L. (2006). The Vertical Structure of Temperature in the Tropics: Different Flavors of El Niño. *Journal of Climate*, 19 (19), 4956-4973. https://doi.org/10.1175/JCLI3891.1

Trenberth, K. E. and Smith, L. (2009). Variations in the three-dimensional structure of the atmospheric circulation with different flavors of El Niño. *Journal of Climate*, 22 (11), 2978–2991. https://doi.org/10.1175/2008JCLI2691.1

Vergados, P., Ao, C. O., Mannucci, A. J. & Kursinski, E. R. (2021). Quantifying the Tropical Upper Tropospheric Warming Amplification Using Radio Occultation Measurements.

Earth and Space Science, 8 (2), e2020EA001597. https://doi.org/10.1029/2020EA001597

WMO (1957): Definition of the tropopause, World Meteorological Organization Bulletin, 6, 136.

Zeng, Z., Sokolovskiy, S., Schreiner, W. S. & Hunt, D. (2019). Representation of vertical atmospheric structures by radio occultation observations in the upper troposphere and lower stratosphere: Comparison to high-resolution radiosonde profiles. *Journal of Atmospheric and Oceanic Technology*, 36 (4), 655–670, https://doi.org/10.1175/JTECH-D-18-0105.1

Zhao, Y. & Li, J. (2006). Discrepancy of mass transport between the Northern and Southern Hemispheres among the ERA-40, NCEP/NCAR, NCEP-DOE AMIP-2, and JRA-25 reanalysis. *Geophysical Research Letters*, 33 (20), L20804. https://doi.org/10.1029/2006GL027287

Zou, C.-Z., Xu, H., Hao, X., & Liu, Q. (2023). Mid-tropospheric layer temperature record derived from satellite microwave sounder observations with backward merging approach. *Journal of Geophysical Research: Atmospheres*, 128 (6), e2022JD037472. https://doi.org/10.1029/2022JD037472.

Figure 1-18.

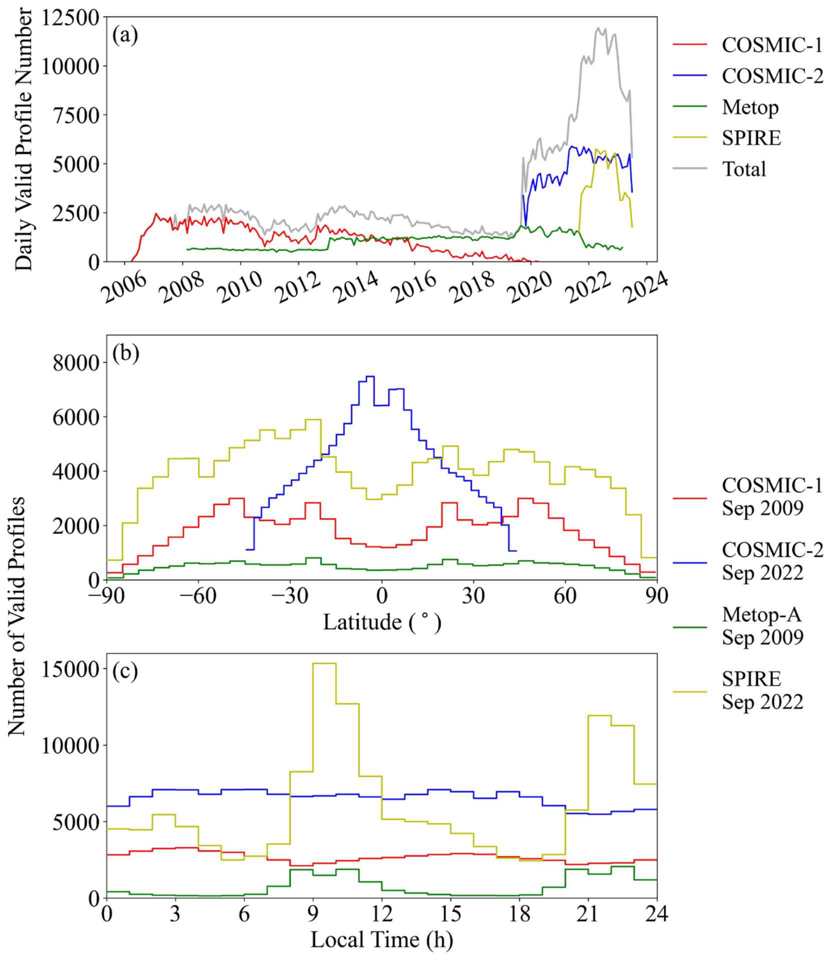
Daily Valid Profile Number
(a)
COSMIC-1
COSMIC-2
Metop
SPIRE
Total
(b)
Latitude (°)
Number of Valid Profiles
COSMIC-1
Sep 2009
COSMIC-2
Sep 2022
Metop-A
Sep 2009
SPIRE
Sep 2022
(c)
Local Time (h)

Figure 1

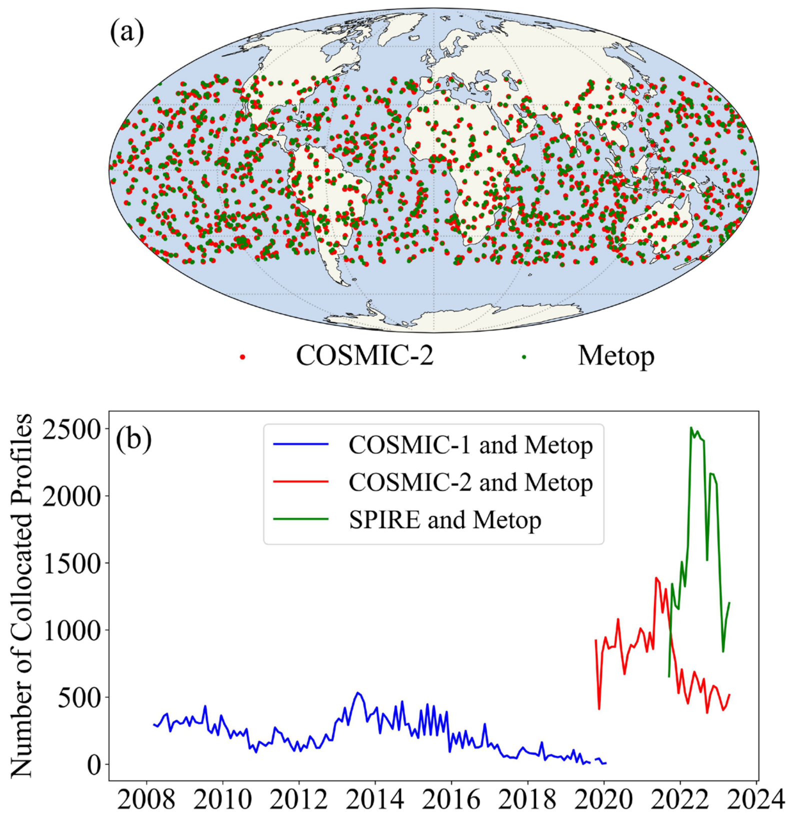
(a)
COSMIC-2
Metop
(b)
COSMIC-1 and Metop
COSMIC-2 and Metop
SPIRE and Metop
Number of Collocated Profiles
0
500
1000
1500
2000
2500
2008
2010
2012
2014
2016
2018
2020
2022
2024

Figure 2

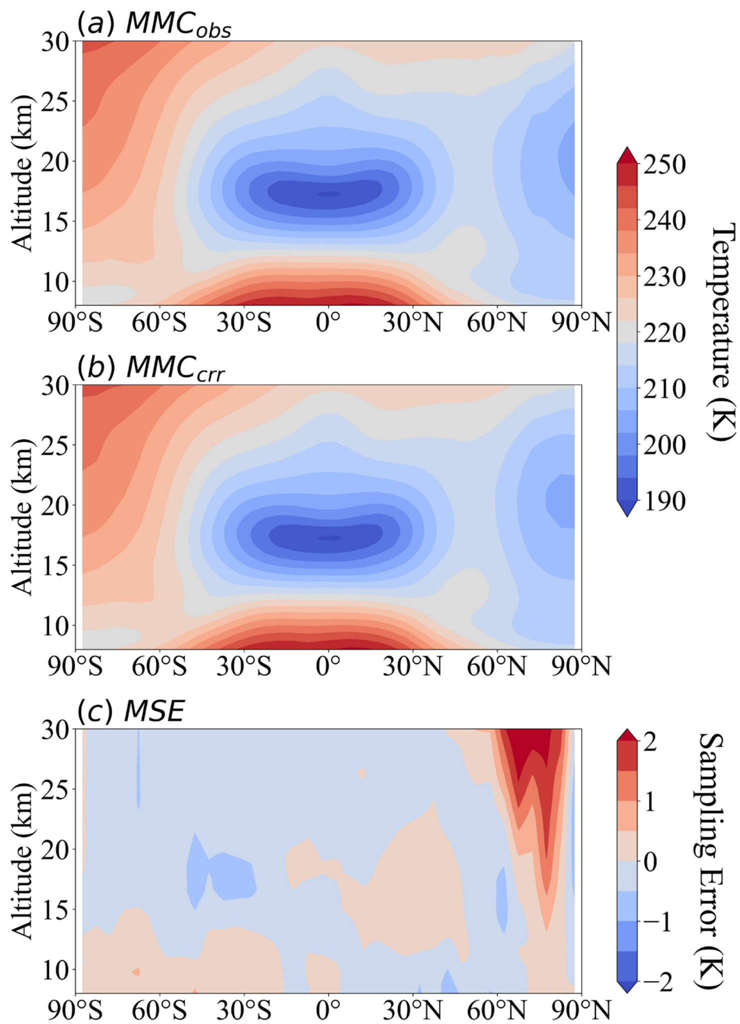
(a) MMC_{obs}
(b) MMC_{crr}
(c) MSE
Altitude (km)
30
25
20
15
10
90°S
60°S
30°S
0°
30°N
60°N
90°N
250
240
230
220
210
200
190
Temperature (K)
2
1
0
−1
−2
Sampling Error (K)

Figure 3

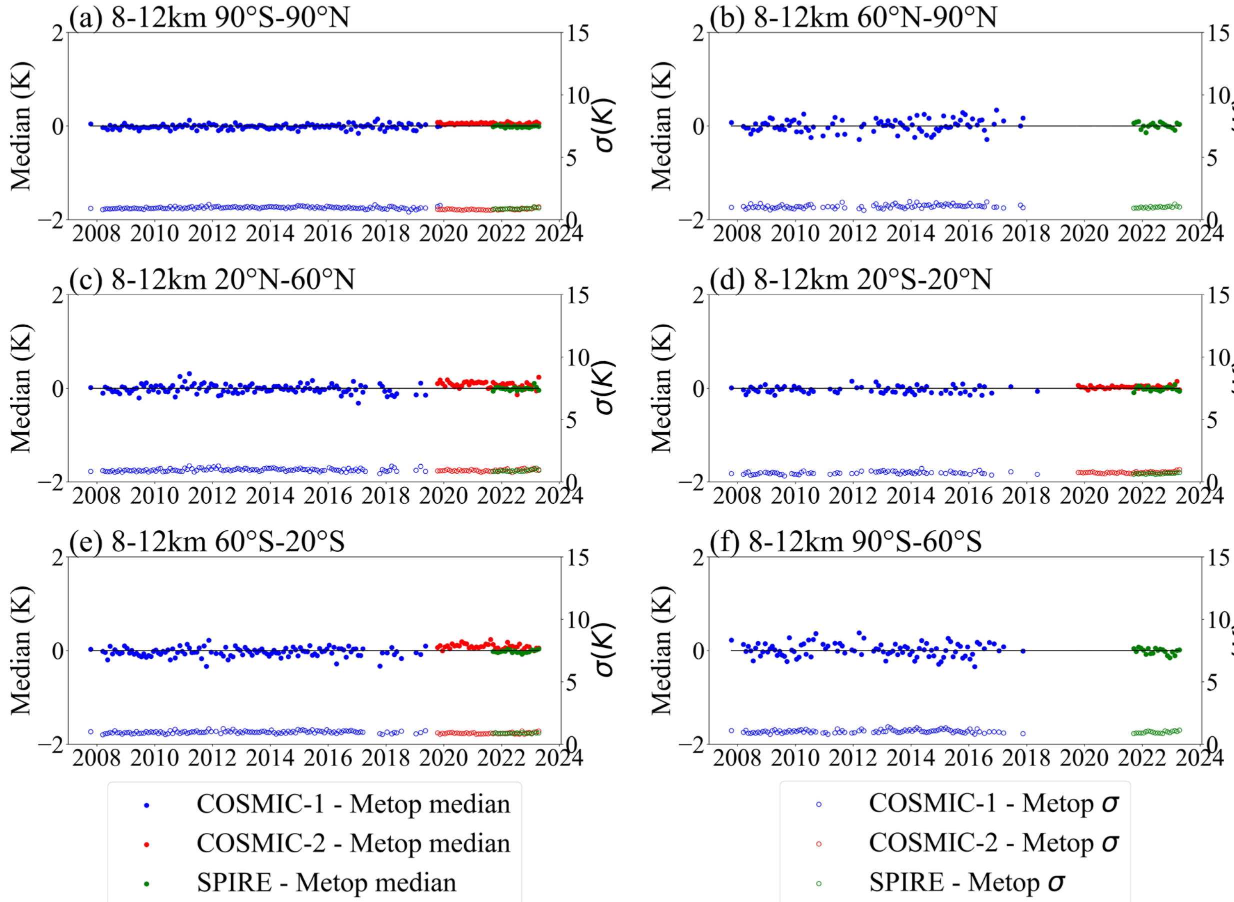
(a) 8-12km 90°S-90°N
(b) 8-12km 60°N-90°N
(c) 8-12km 20°N-60°N
(d) 8-12km 20°S-20°N
(e) 8-12km 60°S-20°S
(f) 8-12km 90°S-60°S
Median (K)
σ(K)
COSMIC-1 - Metop median
COSMIC-2 - Metop median
SPIRE - Metop median
COSMIC-1 - Metop σ
COSMIC-2 - Metop σ
SPIRE - Metop σ

Figure 4

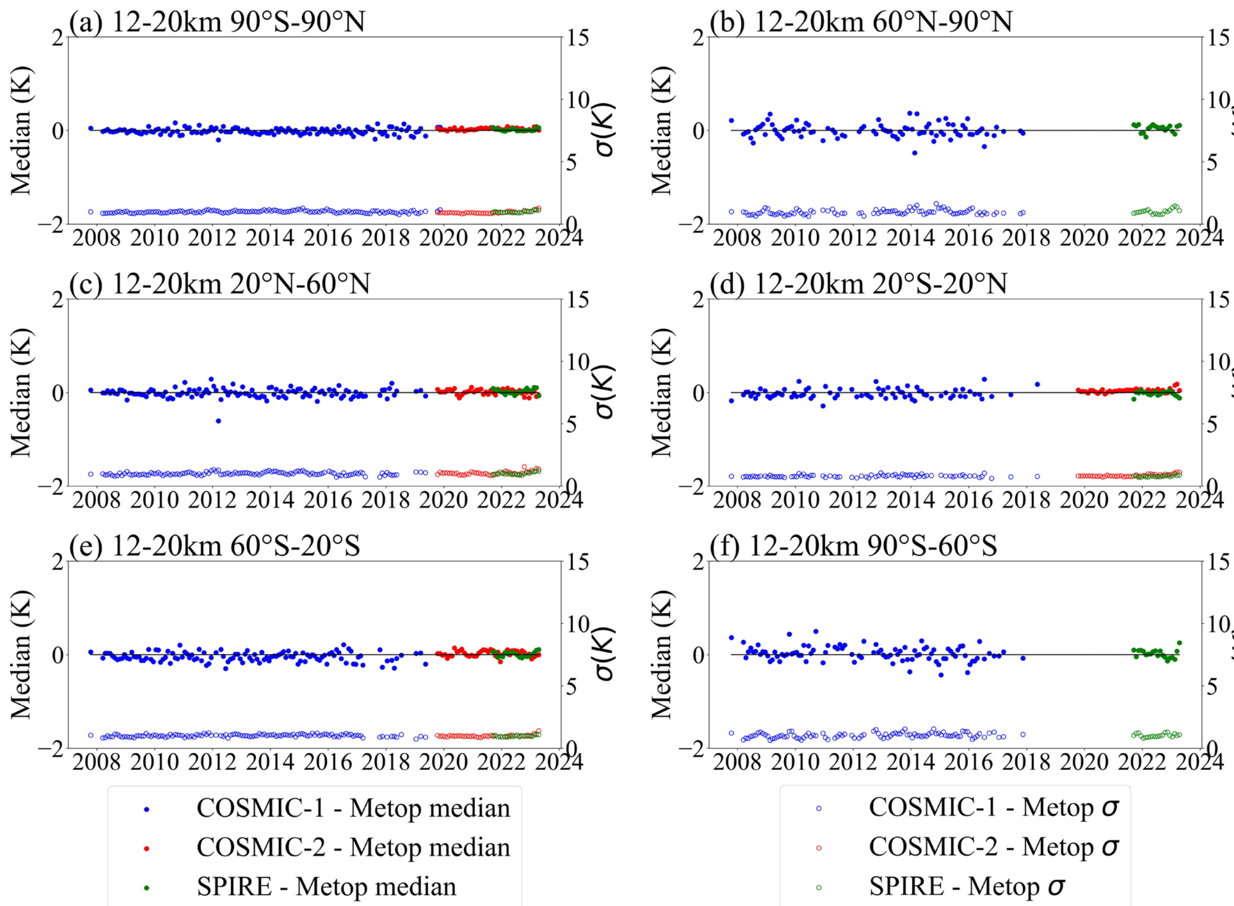
(a) 12-20km 90°S-90°N
(b) 12-20km 60°N-90°N
(c) 12-20km 20°N-60°N
(d) 12-20km 20°S-20°N
(e) 12-20km 60°S-20°S
(f) 12-20km 90°S-60°S
Median (K)
σ(K)
COSMIC-1 - Metop median
COSMIC-2 - Metop median
SPIRE - Metop median
COSMIC-1 - Metop σ
COSMIC-2 - Metop σ
SPIRE - Metop σ

Figure 5

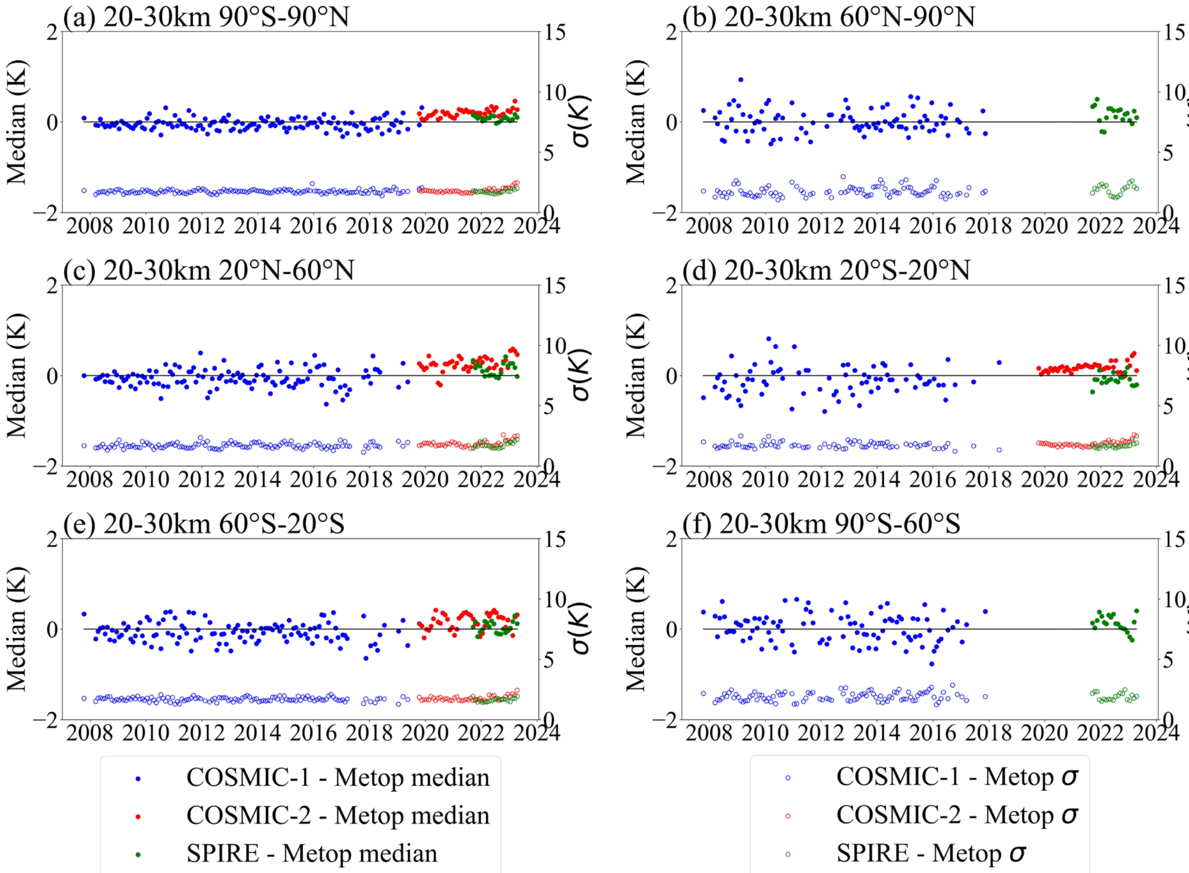
(a) 20-30km 90°S-90°N
(b) 20-30km 60°N-90°N
(c) 20-30km 20°N-60°N
(d) 20-30km 20°S-20°N
(e) 20-30km 60°S-20°S
(f) 20-30km 90°S-60°S
Median (K)
σ(K)
COSMIC-1 - Metop median
COSMIC-2 - Metop median
SPIRE - Metop median
COSMIC-1 - Metop σ
COSMIC-2 - Metop σ
SPIRE - Metop σ

Figure 6

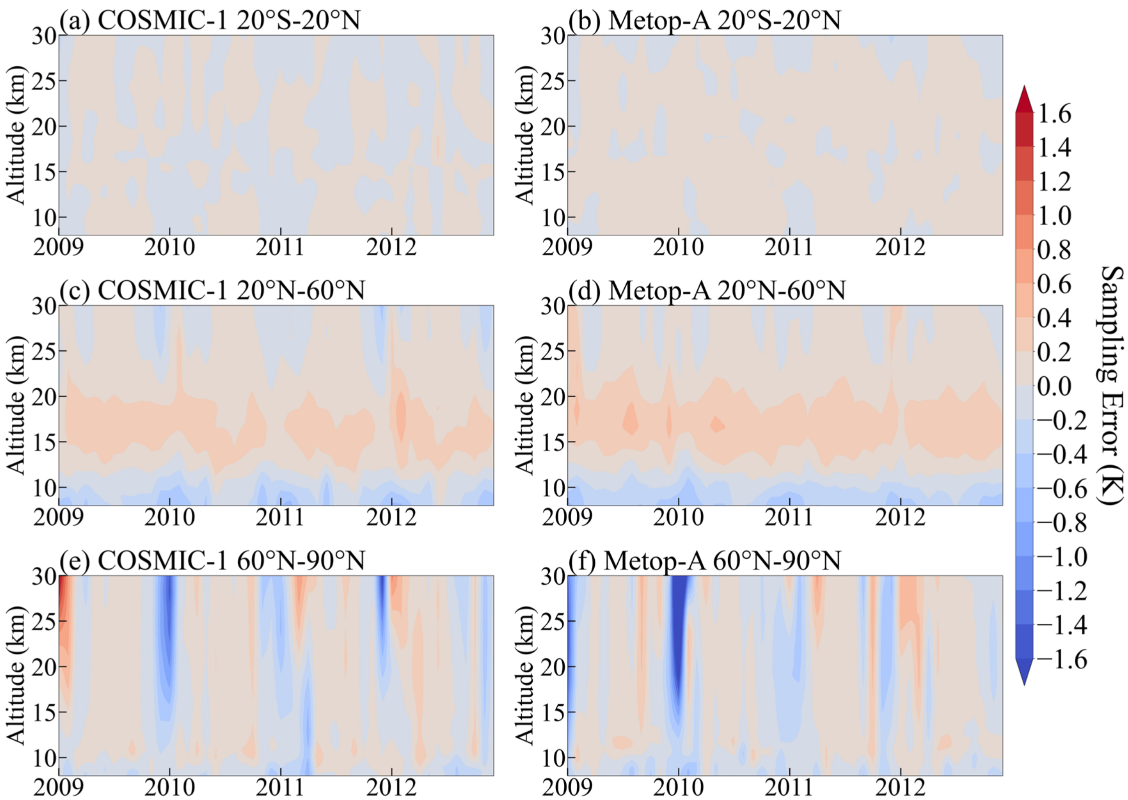
(a) COSMIC-1 20°S-20°N
(b) Metop-A 20°S-20°N
(c) COSMIC-1 20°N-60°N
(d) Metop-A 20°N-60°N
(e) COSMIC-1 60°N-90°N
(f) Metop-A 60°N-90°N
Altitude (km)
10
15
20
25
30
2009
2010
2011
2012
Sampling Error (K)
1.6
1.4
1.2
1.0
0.8
0.6
0.4
0.2
0.0
−0.2
−0.4
−0.6
−0.8
−1.0
−1.2
−1.4
−1.6

Figure 7

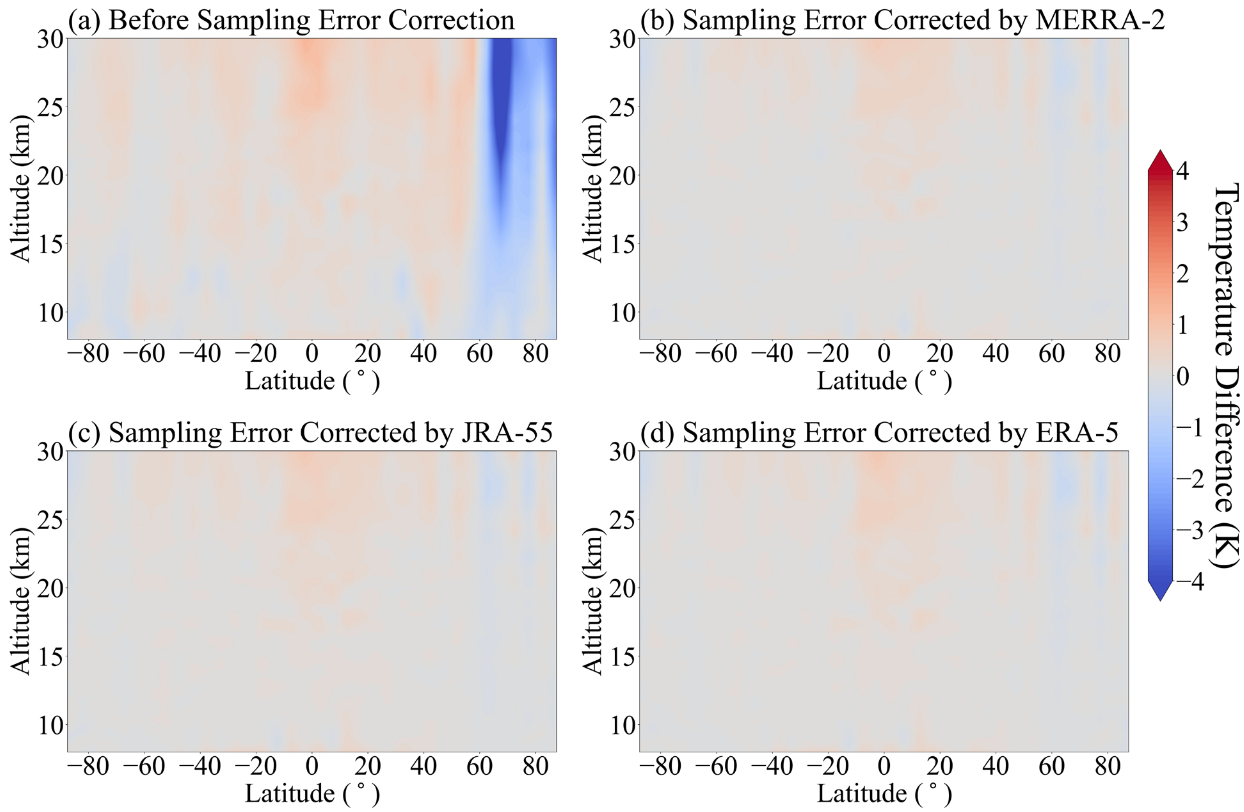
(a) Before Sampling Error Correction
(b) Sampling Error Corrected by MERRA-2
(c) Sampling Error Corrected by JRA-55
(d) Sampling Error Corrected by ERA-5
Altitude (km)
Latitude (°)
Temperature Difference (K)

Figure 8

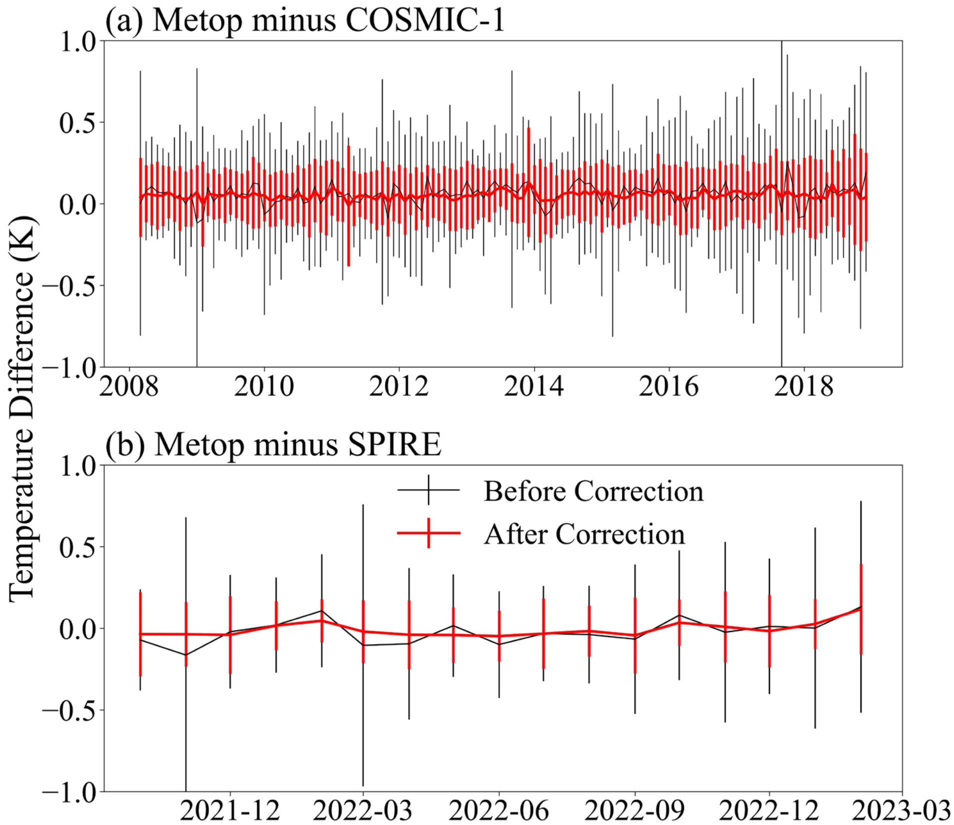
(a) Metop minus COSMIC-1
1.0
0.5
0.0
−0.5
−1.0
2008
2010
2012
2014
2016
2018
Temperature Difference (K)
(b) Metop minus SPIRE
Before Correction
After Correction
1.0
0.5
0.0
−0.5
−1.0
2021-12
2022-03
2022-06
2022-09
2022-12
2023-03

Figure 9

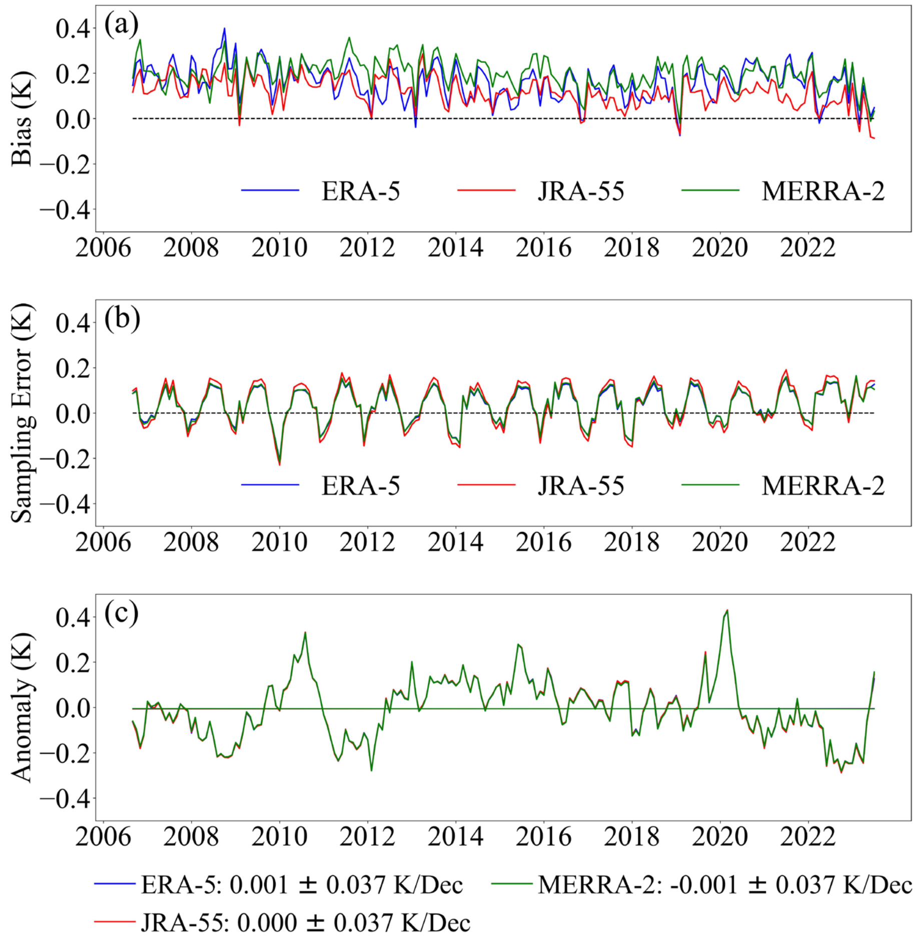

(a)
Bias (K)
0.4
0.2
0.0
−0.2
−0.4
ERA-5
JRA-55
MERRA-2
2006
2008
2010
2012
2014
2016
2018
2020
2022
(b)
Sampling Error (K)
(c)
Anomaly (K)
ERA-5: 0.001 ± 0.037 K/Dec
MERRA-2: -0.001 ± 0.037 K/Dec
JRA-55: 0.000 ± 0.037 K/Dec

Figure 10

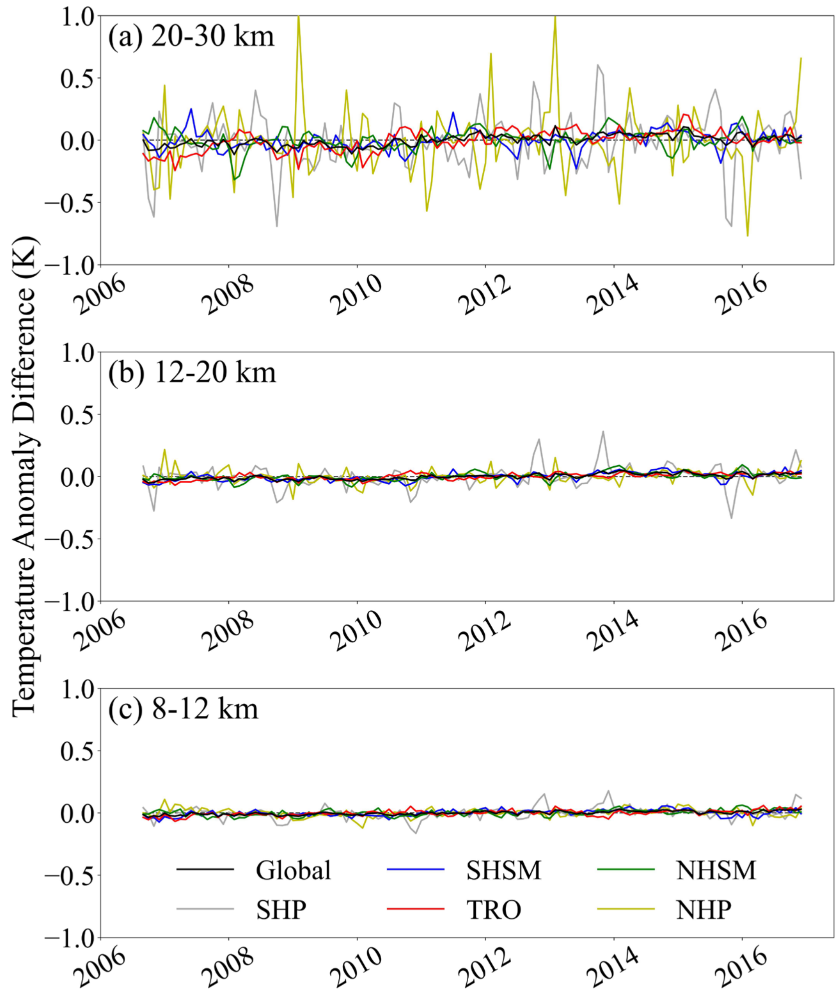
Temperature Anomaly Difference (K)
(a) 20-30 km
(b) 12-20 km
(c) 8-12 km
1.0
0.5
0.0
−0.5
−1.0
2006
2008
2010
2012
2014
2016
Global
SHSM
NHSM
SHP
TRO
NHP

Figure 11

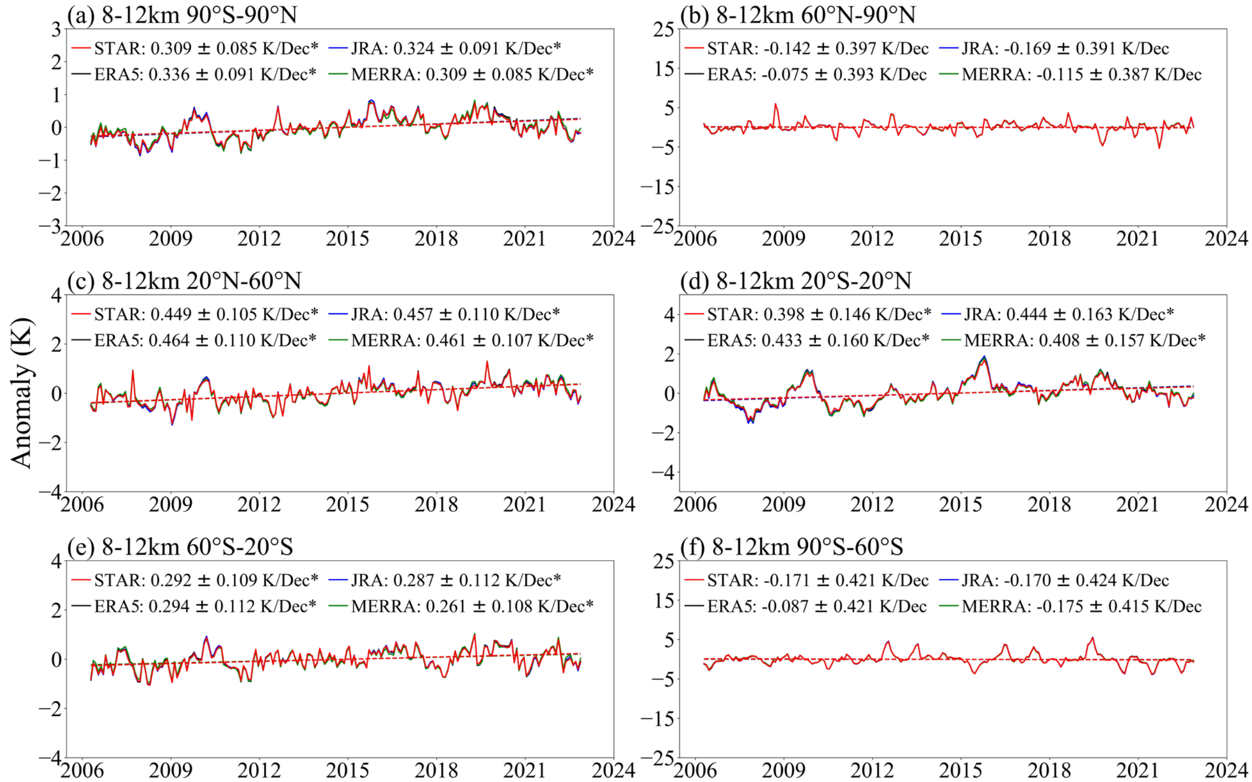
(a) 8-12km 90°S-90°N
STAR: 0.309 ± 0.085 K/Dec*
JRA: 0.324 ± 0.091 K/Dec*
ERA5: 0.336 ± 0.091 K/Dec*
MERRA: 0.309 ± 0.085 K/Dec*
(b) 8-12km 60°N-90°N
STAR: -0.142 ± 0.397 K/Dec
JRA: -0.169 ± 0.391 K/Dec
ERA5: -0.075 ± 0.393 K/Dec
MERRA: -0.115 ± 0.387 K/Dec
(c) 8-12km 20°N-60°N
STAR: 0.449 ± 0.105 K/Dec*
JRA: 0.457 ± 0.110 K/Dec*
ERA5: 0.464 ± 0.110 K/Dec*
MERRA: 0.461 ± 0.107 K/Dec*
(d) 8-12km 20°S-20°N
STAR: 0.398 ± 0.146 K/Dec*
JRA: 0.444 ± 0.163 K/Dec*
ERA5: 0.433 ± 0.160 K/Dec*
MERRA: 0.408 ± 0.157 K/Dec*
(e) 8-12km 60°S-20°S
STAR: 0.292 ± 0.109 K/Dec*
JRA: 0.287 ± 0.112 K/Dec*
ERA5: 0.294 ± 0.112 K/Dec*
MERRA: 0.261 ± 0.108 K/Dec*
(f) 8-12km 90°S-60°S
STAR: -0.171 ± 0.421 K/Dec
JRA: -0.170 ± 0.424 K/Dec
ERA5: -0.087 ± 0.421 K/Dec
MERRA: -0.175 ± 0.415 K/Dec
Anomaly (K)
2006
2009
2012
2015
2018
2021
2024

Figure 12

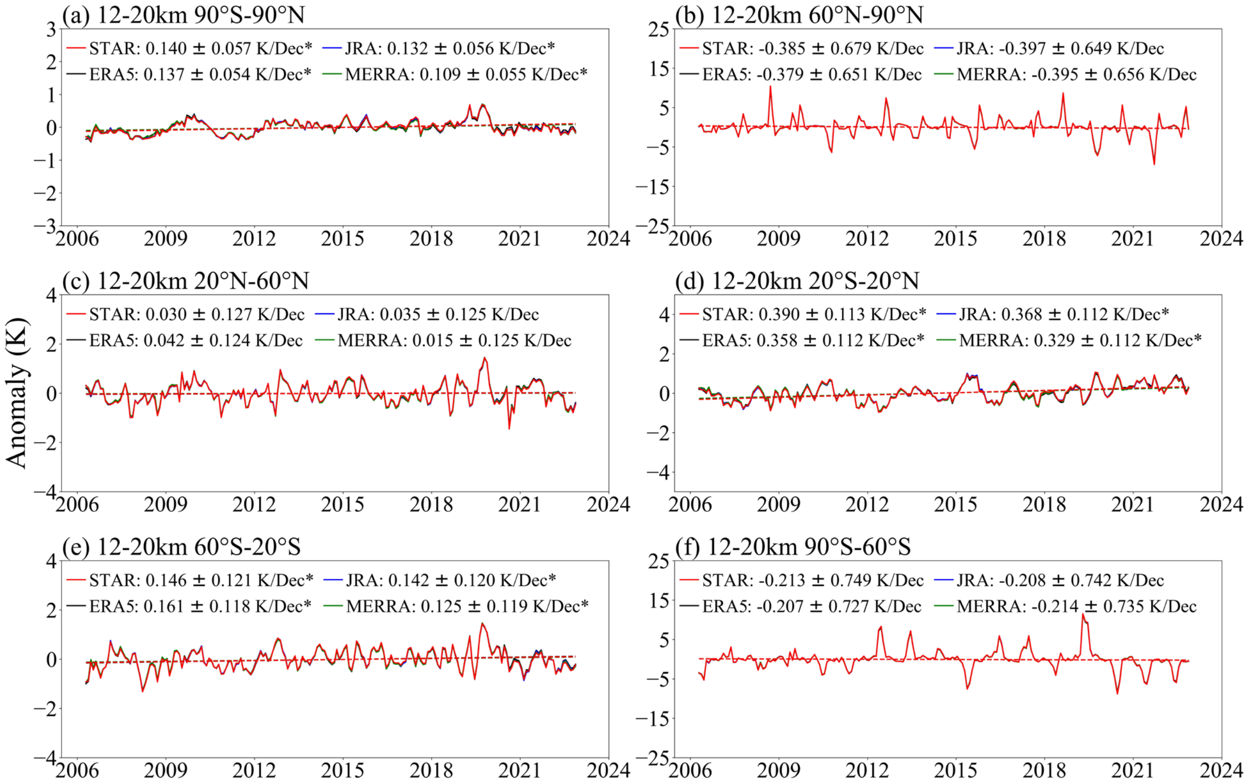
(a) 12-20km 90°S-90°N
STAR: 0.140 ± 0.057 K/Dec*
JRA: 0.132 ± 0.056 K/Dec*
ERA5: 0.137 ± 0.054 K/Dec*
MERRA: 0.109 ± 0.055 K/Dec*
(b) 12-20km 60°N-90°N
STAR: -0.385 ± 0.679 K/Dec
JRA: -0.397 ± 0.649 K/Dec
ERA5: -0.379 ± 0.651 K/Dec
MERRA: -0.395 ± 0.656 K/Dec
(c) 12-20km 20°N-60°N
STAR: 0.030 ± 0.127 K/Dec
JRA: 0.035 ± 0.125 K/Dec
ERA5: 0.042 ± 0.124 K/Dec
MERRA: 0.015 ± 0.125 K/Dec
(d) 12-20km 20°S-20°N
STAR: 0.390 ± 0.113 K/Dec*
JRA: 0.368 ± 0.112 K/Dec*
ERA5: 0.358 ± 0.112 K/Dec*
MERRA: 0.329 ± 0.112 K/Dec*
(e) 12-20km 60°S-20°S
STAR: 0.146 ± 0.121 K/Dec*
JRA: 0.142 ± 0.120 K/Dec*
ERA5: 0.161 ± 0.118 K/Dec*
MERRA: 0.125 ± 0.119 K/Dec*
(f) 12-20km 90°S-60°S
STAR: -0.213 ± 0.749 K/Dec
JRA: -0.208 ± 0.742 K/Dec
ERA5: -0.207 ± 0.727 K/Dec
MERRA: -0.214 ± 0.735 K/Dec
Anomaly (K)
2006
2009
2012
2015
2018
2021
2024

Figure 13

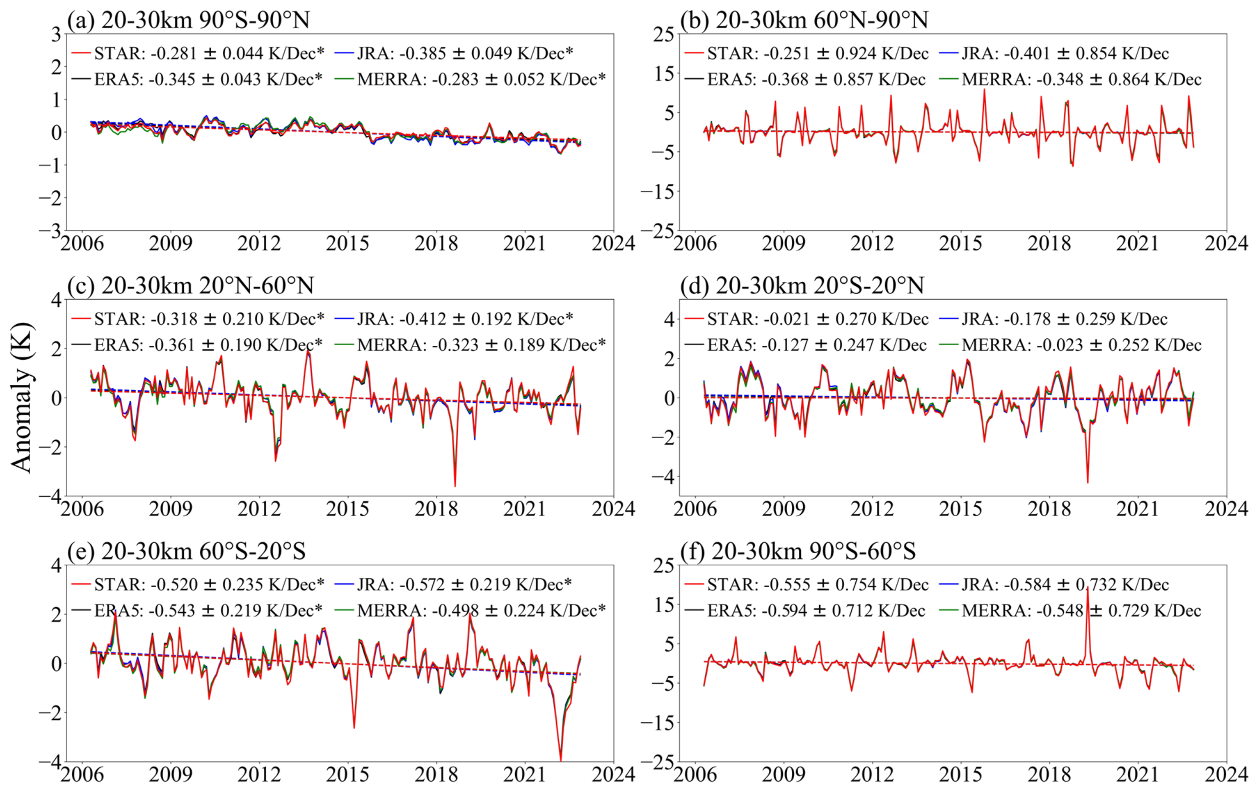
(a) 20-30km 90°S-90°N
STAR: -0.281 ± 0.044 K/Dec*
JRA: -0.385 ± 0.049 K/Dec*
ERA5: -0.345 ± 0.043 K/Dec*
MERRA: -0.283 ± 0.052 K/Dec*
(b) 20-30km 60°N-90°N
STAR: -0.251 ± 0.924 K/Dec
JRA: -0.401 ± 0.854 K/Dec
ERA5: -0.368 ± 0.857 K/Dec
MERRA: -0.348 ± 0.864 K/Dec
(c) 20-30km 20°N-60°N
STAR: -0.318 ± 0.210 K/Dec*
JRA: -0.412 ± 0.192 K/Dec*
ERA5: -0.361 ± 0.190 K/Dec*
MERRA: -0.323 ± 0.189 K/Dec*
(d) 20-30km 20°S-20°N
STAR: -0.021 ± 0.270 K/Dec
JRA: -0.178 ± 0.259 K/Dec
ERA5: -0.127 ± 0.247 K/Dec
MERRA: -0.023 ± 0.252 K/Dec
(e) 20-30km 60°S-20°S
STAR: -0.520 ± 0.235 K/Dec*
JRA: -0.572 ± 0.219 K/Dec*
ERA5: -0.543 ± 0.219 K/Dec*
MERRA: -0.498 ± 0.224 K/Dec*
(f) 20-30km 90°S-60°S
STAR: -0.555 ± 0.754 K/Dec
JRA: -0.584 ± 0.732 K/Dec
ERA5: -0.594 ± 0.712 K/Dec
MERRA: -0.548 ± 0.729 K/Dec
Anomaly (K)
2006
2009
2012
2015
2018
2021
2024

Figure 14

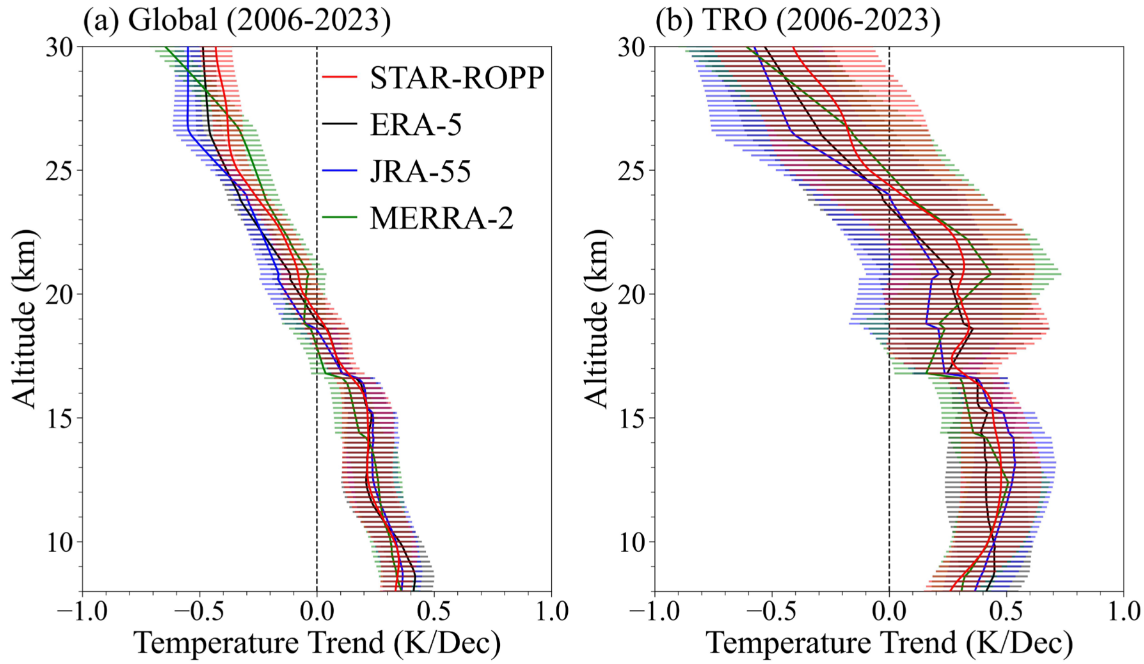
(a) Global (2006-2023)
(b) TRO (2006-2023)
STAR-ROPP
ERA-5
JRA-55
MERRA-2
Altitude (km)
Temperature Trend (K/Dec)
30
25
20
15
10
−1.0
−0.5
0.0
0.5
1.0

Figure 15

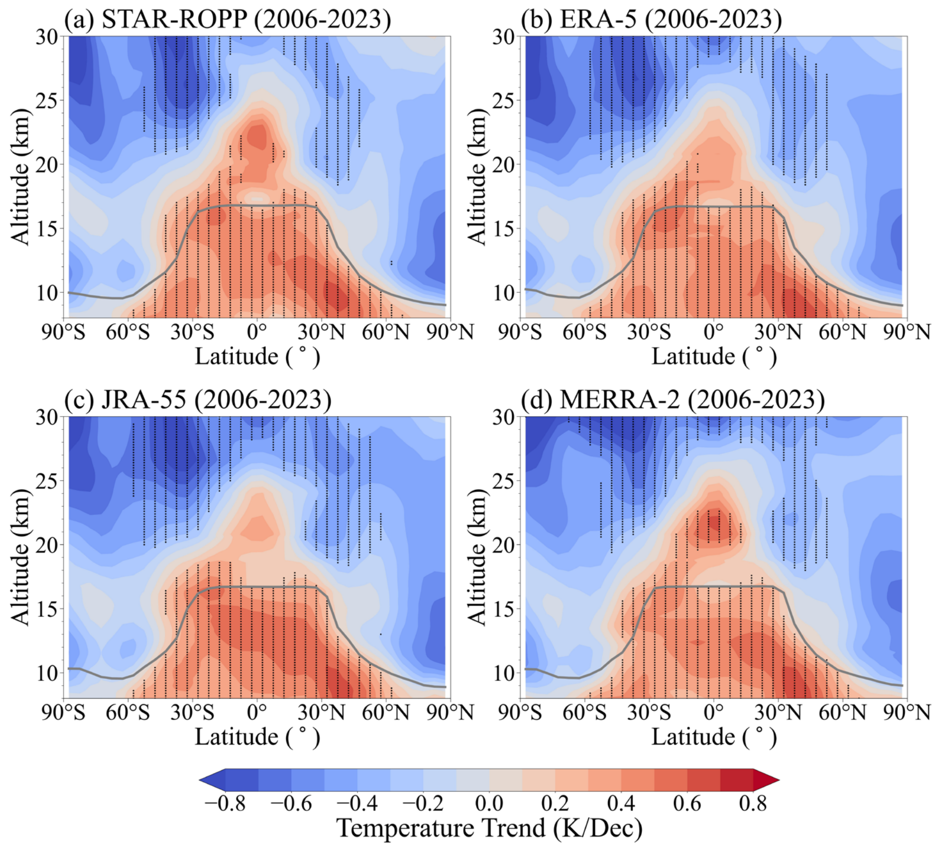
(a) STAR-ROPP (2006-2023)
(b) ERA-5 (2006-2023)
(c) JRA-55 (2006-2023)
(d) MERRA-2 (2006-2023)
Altitude (km)
30
25
20
15
10
90°S 60°S 30°S 0° 30°N 60°N 90°N
Latitude (°)
−0.8 −0.6 −0.4 −0.2 0.0 0.2 0.4 0.6 0.8
Temperature Trend (K/Dec)

Figure 16

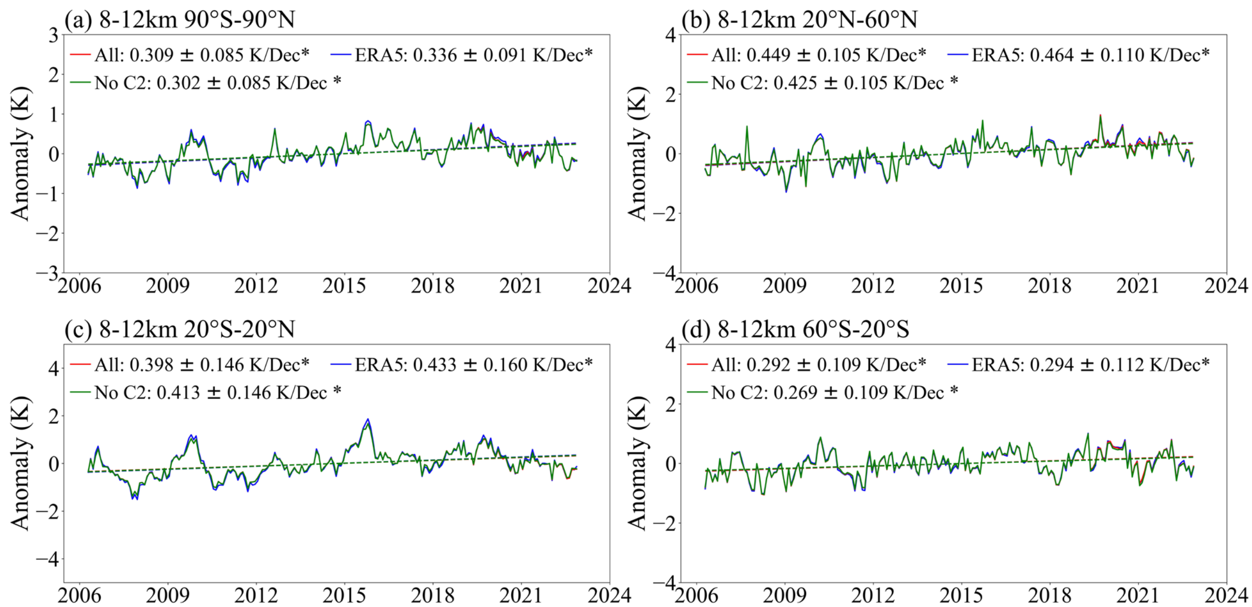
(a) 8-12km 90°S-90°N
All: 0.309 ± 0.085 K/Dec*
ERA5: 0.336 ± 0.091 K/Dec*
No C2: 0.302 ± 0.085 K/Dec *
(b) 8-12km 20°N-60°N
All: 0.449 ± 0.105 K/Dec*
ERA5: 0.464 ± 0.110 K/Dec*
No C2: 0.425 ± 0.105 K/Dec *
(c) 8-12km 20°S-20°N
All: 0.398 ± 0.146 K/Dec*
ERA5: 0.433 ± 0.160 K/Dec*
No C2: 0.413 ± 0.146 K/Dec *
(d) 8-12km 60°S-20°S
All: 0.292 ± 0.109 K/Dec*
ERA5: 0.294 ± 0.112 K/Dec*
No C2: 0.269 ± 0.109 K/Dec *
Anomaly (K)
2006
2009
2012
2015
2018
2021
2024

Figure 17

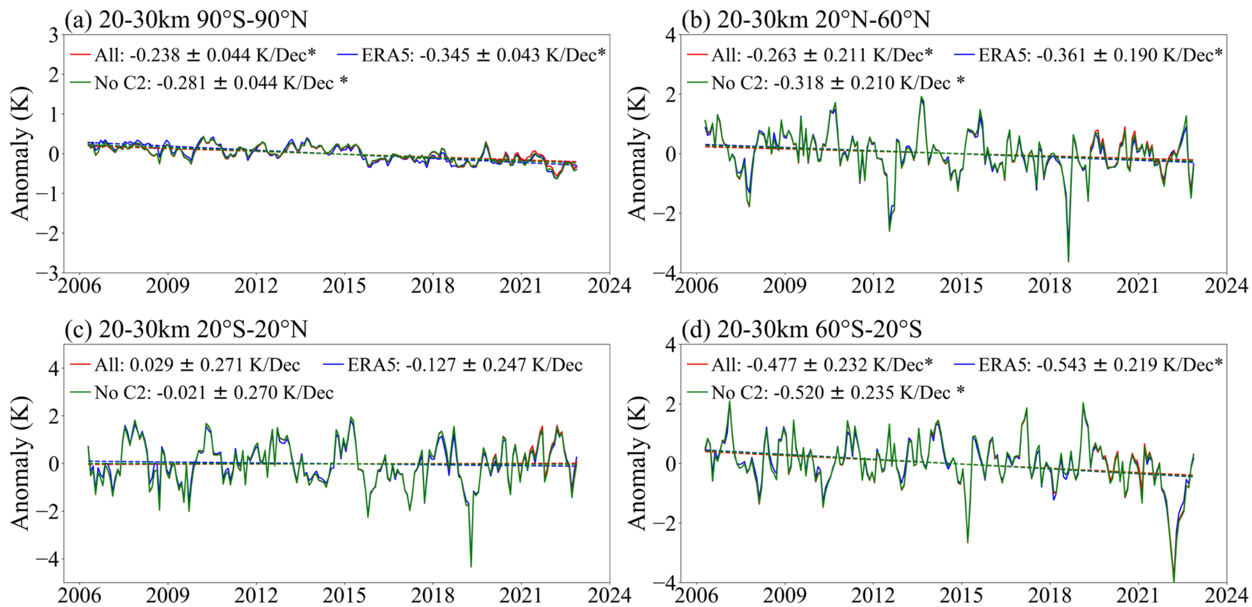
(a) 20-30km 90°S-90°N
All: -0.238 ± 0.044 K/Dec*
ERA5: -0.345 ± 0.043 K/Dec*
No C2: -0.281 ± 0.044 K/Dec *
(b) 20-30km 20°N-60°N
All: -0.263 ± 0.211 K/Dec*
ERA5: -0.361 ± 0.190 K/Dec*
No C2: -0.318 ± 0.210 K/Dec *
(c) 20-30km 20°S-20°N
All: 0.029 ± 0.271 K/Dec
ERA5: -0.127 ± 0.247 K/Dec
No C2: -0.021 ± 0.270 K/Dec
(d) 20-30km 60°S-20°S
All: -0.477 ± 0.232 K/Dec*
ERA5: -0.543 ± 0.219 K/Dec*
No C2: -0.520 ± 0.235 K/Dec *
Anomaly (K)
2006
2009
2012
2015
2018
2021
2024

Figure 18